Spin-orbit induced noncubic charge distribution in cubic ferromagnets. I. Electric field gradient measurements on 5*d* impurities in Fe and Ni

G. Seewald, E. Hagn, and E. Zech
Physik-Department, Technische Universität München, D-85748 Garching, Germany

R. Kleyna and M. Voß
Institut für Physikalische und Theoretische Chemie, Universität Erlangen-Nürnberg, D-91058 Erlangen, Germany

A. Burchard
PPE Division, CERN, CH-1211 Geneva 23, Switzerland

ISOLDE Collaboration
CERN, CH-1211 Geneva 23, Switzerland

(Received 6 April 2002; published 4 November 2002)

The spin-orbit induced electric field gradient at the nuclear site of ^{183}Os and ^{183}Re impurities in Fe and of ^{191}Pt and ^{186}Ir impurities in Ni was determined for [100], [110], and [111] orientations of the magnetization. The measurements were performed on single-crystal samples using nuclear magnetic resonance on oriented nuclei and modulated adiabatic fast passage on oriented nuclei. In the Ni experiments the electric field gradient was also determined for other orientations of the magnetization in the (110) plane. These data, together with previous results on the 5*d* impurities, provide the first fairly complete data set on the spin-orbit induced electric field gradient in cubic Fe, Co, and Ni. Our results establish in particular that the effect depends in general considerably on the direction of the magnetization. We summarize the present knowledge of these electric field gradients, their magnitude, their systematics, and the form and magnitude of their dependence on the direction of the magnetization. The properties of the effect are explained within the tight-binding model in terms of the spin-orbit induced deformation of the electron distribution. We also present and discuss data on the dependence of the hyperfine field on the direction of the magnetization, which was found to be smaller than 10^{-3}, and on the inhomogeneous broadening of the electric field gradient.

DOI: 10.1103/PhysRevB.66.174401 PACS number(s): 75.50.Bb, 76.60.Jx, 76.60.Gv, 76.80.+y

I. INTRODUCTION

The spin-orbit coupling (SOC) induces in ferromagnetic transition metals not only the well-known unquenched orbital moment but deforms also the spatial electron distribution. This leads in ferromagnets with cubic lattice symmetry to a noncubic charge distribution. The effect can be studied via the hyperfine interaction: The electric field gradient (EFG) at the nuclear site is a direct measure of the noncubic charge distribution around the nucleus.

The EFG in cubic ferromagnets was first observed on Ir as a dilute impurity in Fe (Ir*Fe*) and also on Ir*Ni* and Fe*Fe* by various techniques.[1–4] It was explained as a consequence of the spin-orbit coupling.[1,5–7] The spin-orbit EFG (SO-EFG) was observed since then for several other impurity host combinations,[8–10] but precise data remained until recently restricted to only a few favorable systems. The main problem was that the quadrupole splitting of the nuclear magnetic resonance due to the SO-EFG is in most cases concealed by a much larger inhomogeneous broadening of the resonance.

However, this problem has meanwhile been solved by the introduction of the technique of modulated adiabatic fast passage on oriented nuclei (MAPON).[11,12] The modulated adiabatic fast passage concept allows the determination of the quadrupole splitting, even if it is much smaller than the inhomogeneous broadening of the resonance. MAPON combines this concept with the detection of the resonance via the γ radiation of radioactive probe nuclei. The high sensitivity of the technique greatly facilitates the study of the hyperfine interaction at impurities, especially in single-crystal samples.

But the first MAPON experiments revealed further difficulties, which had not been noticed in previous studies, but which now became apparent due to the improved resolution. One difficulty was the strong inhomogeneous broadening of the SO-EFG: If it exceeds considerably 100%, a precise determination of the SO-EFG is no longer possible and the MAPON experiment gives essentially only the width of the EFG distribution. This has so far been the case in all MAPON experiments on 3*d* and 4*sp* impurities in Fe and Ni.[13–16] The only exception was Co*Fe*. In that case the SO-EFG could be determined with moderate precision for [100] orientation of the magnetization.[17,18]

A second difficulty was the neglect of the anisotropy of the SO-EFG—that is, the dependence of the effect on the direction of the magnetization relative to the crystallographic axes. Model calculations predicted a distinct anisotropy of the order of 50%.[7] But in two experiments on Ir*Fe* and Ir*Ni* the SO-EFG was found to be isotropic within the experimental error of about 10%.[2,5] The SO-EFG was since then believed to be essentially isotropic.

Recent MAPON experiments provided, however, strong hints at a distinct anisotropy of the SO-EFG: In some experiments on 3*d* and 4*sp* impurities in single-crystal samples different EFG distributions were observed for different directions of the magnetization.[13,14,19] Because of the excessive inhomogeneous broadening, it was, however, not clear

whether this anisotropy is due to the SO-EFG or due to additional contributions to the EFG that cause also the inhomogeneous broadening. A further hint came from experiments on the $5d$ impurities Au and Ir in polycrystalline Fe samples.[20,21] The average SO-EFG was found to be magnetic field dependent in the regime of incomplete magnetization, where the direction of the magnetization is also magnetic field dependent. This pointed also to an anisotropy of the SO-EFG. The broadening of the EFG was in this case less than 100%, but an unambiguous distinction between an anisotropy and a real magnetic field dependence is not possible for polycrystalline samples.

From this experience the requirements for further experiments were clear: For a proper treatment of the anisotropy single-crystal samples were necessary. To reduce the inhomogeneous broadening of the SO-EFG to a tolerable extent much attention had to be paid to the sample preparation. The SO-EFG of the $5d$ impurities was obviously less affected by the inhomogeneous broadening, presumably because the SOC is an order of magnitude larger than for the $4d$ or $3d$ impurities. Therefore we used the $5d$ impurities as the starting point.

Using NMR-ON (nuclear magnetic resonance on oriented nuclei) and MAPON we determined the SO-EFG of AuFe, PtFe, IrFe, OsFe, ReFe, AuNi, PtNi, and IrNi for [100], [110], and [111] orientations of the magnetization. In addition, the average SO-EFG of Pt, Ir, Os, and Re in Co(fcc) was determined. Now, for the first time a reasonably complete and accurate data set is available to investigate the systematics and the anisotropy of the noncubic charge distribution in cubic Fe, Co, and Ni.

The experiment on IrFe provided the first unambiguous evidence for the anisotropy of the SO-EFG. It was already discussed in Ref. 22. The measurements on PtFe were reported in Ref. 23, the measurements on the $5d$ impurities in Co(fcc) in Ref. 24. A complete account of the experiments on OsFe, ReFe, PtNi, and IrNi is given in Sec. IV. The physics of the spin-orbit induced noncubic charge distribution is discussed in Sec. V on the basis of the tight-binding analysis that is presented in the following paper (part II).[25]

II. EXPERIMENTAL METHODS

A. Hyperfine interaction in cubic Fe, Co, and Ni

In Fe, Co, and Ni the electric hyperfine interaction between the SO-EFG and nuclear quadrupole moment is superimposed onto a much stronger magnetic hyperfine interaction between hyperfine field and nuclear magnetic moment. The sublevel energies E_m of a nuclear state with spin I are given by

$$E_m = -g\mu_N B m + \frac{eQV_{z'z'}}{4I(2I-1)}[3m^2 - I(I+1)]. \qquad (1)$$

The sublevels are eigenfunctions of $I_{z'}$. The z' axis is the direction of $\vec{B}$, the effective magnetic field at the nuclear site. It is referred to as z' to distinguish it from the cubic axes x, y, and z. m is the magnetic quantum number, g the nuclear g factor, μ_N the nuclear magneton, eQ the nuclear spectroscopic quadrupole moment, and $V_{z'z'}$ the component of the EFG tensor along $\vec{B}$.

According to Eq. (1) the resonance frequency of the NMR transition between the sublevels $|m\rangle$ and $|m+1\rangle$ is given by

$$\nu_{m\to m+1} = \nu_m + \Delta\nu_Q(m+\tfrac{1}{2}), \qquad (2)$$

$$\nu_m = |g\mu_N B/h|, \qquad (3)$$

$$\Delta\nu_Q = \frac{3}{2I(2I-1)}\frac{eQV_{z'z'}}{h}. \qquad (4)$$

Thus, there is a quadrupole splitting of the magnetic resonance at ν_m into $2I$ equidistant subresonances with subresonance separation $\Delta\nu_Q$. $\Delta\nu_Q$ is the central quantity in this work since it provides the desired information on the noncubic charge distribution.

$\vec{B}$ is the sum of the hyperfine field $\vec{B}_{\rm HF}$, the external magnetic field $\vec{B}_{\rm ext}$, and the demagnetization field. If all fields are parallel to the magnetization, which was fulfilled in this work for all measurements of the magnetic hyperfine interaction, ν_m is given by

$$\nu_m = \nu_m^{(0)} + (d\nu/dB_{\rm ext})B_0, \qquad (5)$$

$$\nu_m^{(0)} = |g\mu_N B_{\rm HF}/h|, \qquad (6)$$

$$d\nu/dB_{\rm ext} = |g\mu_N/h|\,{\rm sgn}(B_{\rm HF})(1+K), \qquad (7)$$

$$B_0 = 0 \quad \text{for } B_{\rm ext} < B_{\rm dem},$$

$$B_0 = B_{\rm ext} - B_{\rm dem} \quad \text{for } B_{\rm ext} > B_{\rm dem}. \qquad (8)$$

The zero-field magnetic resonance frequency $\nu_m^{(0)}$ represents the intrinsic magnetic hyperfine interaction. The parameter K takes Knight shift and diamagnetic shielding into account and is of the order of 1%. B_0 is the ''effective'' external magnetic field and includes the shielding by the demagnetization field. $B_{\rm dem}$ is the demagnetization field for the fully magnetized sample. Since our samples were not rotation ellipsoids and the sample shape and the position of the beam spot were in general not exactly symmetric, $B_{\rm dem}$ had to be calculated numerically for each orientation of the magnetization.

Equations (1) and (2) hold exactly only if the EFG is axially symmetric and the main axis is parallel to $\vec{B}$. Due to the anisotropy of the SO-EFG, this is in general fulfilled only for [100] and [111] orientations of the magnetization.[26] However, the spin-orbit induced quadrupole interaction is very small with respect to the magnetic interaction. In this situation, Eq. (1) is true within the experimental accuracy for all directions of the magnetization. This also means that only the $z'z'$ component of the EFG tensor can be deduced from the experiment. Therefore, in the following the quantity $V_{z'z'}$ will be referred to shortly as the SO-EFG.

B. NMR-ON

The magnetic and electric hyperfine interactions were determined by NMR-ON and the related MAPON technique. Both methods make use of the anisotropic γ emission from oriented radioactive probe nuclei. The nuclear spins are thermally oriented in the strong hyperfine fields in Fe and Ni at temperatures in the millikelvin range. For NMR-ON the γ anisotropy is measured as a function of the frequency of the applied radio frequency (rf) field. Resonant deorientations of the nuclear spins are detected via the corresponding change of the γ anisotropy.[27]

To realize the single-impurity limit a low dose of the impurities was mass separator implanted in carefully prepared Fe and Ni single crystals. NMR-ON and MAPON are ideally suited for hyperfine interaction studies on such samples because of the high sensitivity, which allows precise measurements on less than 10^{10} probe nuclei.

The width of the individual subresonances is given in the simplest case by Γ_m, the inhomogeneous broadening of ν_m. If the subresonance splitting $\Delta\nu_Q$ is larger than Γ_m, it can be directly determined from the NMR-ON spectrum. However, if Γ_m is considerably larger than $\Delta\nu_Q$, all subresonances merge into one resonance and $\Delta\nu_Q$ can be determined only by the MAPON method. Apart from some favorable cases, this is the usual situation in cubic Fe, Co, and Ni.

The center of the NMR-ON resonance $\bar{\nu}$ deviates in general from ν_m, because the subresonance amplitudes are not symmetrically distributed around ν_m. This deviation can be still significant even if the subresonance structure is not resolved. To determine ν_m in these cases the NMR-ON spectrum was described as the superposition of the individual subresonances. The distribution of $\Delta\nu_Q$, $P(\Delta\nu_Q)$, was taken from the MAPON measurements. The relative strengths of the subresonance amplitudes were calculated. There are some uncertainties in this procedure: (i) One has to rely on calculated subresonance amplitudes. (ii) The simple superposition of subresonances is only approximately correct if more than one subresonance of a nucleus is excited at the same time. (iii) A Gaussian shape of $P(\nu_m)$ has to be assumed. Therefore, a systematic error of 30% of $\bar{\nu}-\nu_1$ was added to the final result for ν_m. ν_1 is the subresonance between the most occupied sublevels and represents the limit of $\bar{\nu}$ for $T\rightarrow 0$.

C. MAPON

For a full account of the MAPON method we refer to Refs. 11, 12, and 17. MAPON is an extension of the adiabatic fast passage (AFP) technique, where the rf frequency is swept over the resonance in a time that is short with respect to the relaxation time. In the MAPON method *two* rf fields with fixed frequency separation $\Delta\nu$ are swept over the complete resonance structure. There are essentially only two different final states after the MAPON sweep as a function of $\Delta\nu$: one for $\Delta\nu<\Delta\nu_Q$ and the other for $\Delta\nu>\Delta\nu_Q$. The final state is in particular independent of ν_m. In this way the influence of the inhomogeneous broadening of the magnetic hyperfine splitting is eliminated.

The "MAPON spectrum" is the γ anisotropy after the sweep as a function of $\Delta\nu$. For a uniform quadrupole splitting it is simply a step function with step at $\Delta\nu=\Delta\nu_Q$. However, it turned out that $\Delta\nu_Q$ is also inhomogeneously broadened. The MAPON spectrum is then, apart from some constants, the integral over the distribution $P(\Delta\nu_Q)$.

To determine $\Delta\nu_Q^{(0)}$, the quadrupole splitting that represents the undisturbed system, we assumed a Gaussian distribution of $\Delta\nu_Q$ and described the MAPON spectrum as the integral over $P(\Delta\nu_Q)$. The center $\Delta\nu_Q^{(0)}$ and width Γ_Q of the distribution were determined via a *least-squares fit*. If necessary, a second, much broader, Gaussian distribution was introduced to describe a broad background due to nuclei with somewhat more disturbed surroundings.

Only the MAPON spectrum was used to obtain the final results. But in most cases the first derivative of the MAPON spectrum is also shown to provide a picture of $P(\Delta\nu_Q)$. There are several reasonable ways to differentiate the MAPON spectrum. We plot in this work

$$(E_{i+n}-E_i)/(\Delta\nu_{i+n}-\Delta\nu_i)$$

as a function of $(\Delta\nu_{i+n}+\Delta\nu_i)/2$. This quantity is strictly speaking only the average of the derivative over the interval $(\Delta\nu_{i+n}-\Delta\nu_i)$. E_i is the MAPON effect at the ith data point. n is chosen in a way to achieve a reasonable compromise between the accuracy of each point and the error introduced by the averaging. The used n's range in this work from 2 to 4.

The 1:1 correspondence between the MAPON spectrum and the integral of $P(\Delta\nu_Q)$ is not exact. The power broadening[12] and the nuclear spin-lattice relaxation during the MAPON sweep modify this simple relationship and introduce a slight deviation of the center of the MAPON spectrum from the center of $P(\Delta\nu_Q)$. The deviation can be reduced by an appropriate choice of the rf power and the sweep time to less than $\sqrt{d\nu/dt}$, where $d\nu/dt$ is the MAPON sweep rate.[28] The quoted $\Delta\nu_Q^{(0)}$'s contain already appropriate corrections that were estimated by model calculations.[12,28] These corrections are, however, small: Even for $^{183}\mathrm{Re}Fe$ and $^{186}\mathrm{Ir}Ni$, where large sweep rates were necessary because of the fast nuclear spin-lattice relaxation, the corrections were only of the same order as the statistical error.

D. Sign of the quadrupole splitting

According to Eq. (2), the subresonance between the most occupied sublevels is situated at the low-frequency end of the resonance for $\Delta\nu_Q>0$ and at the high-frequency end for $\Delta\nu_Q<0$. Moreover, the NMR-ON technique is characterized by a strong decrease in the occupation numbers from the best occupied sublevel to higher sublevels, which leads to a corresponding strong decrease in the amplitudes of the associated subresonances. Therefore, the sign of the quadrupole splitting can be directly read off the arrangement of the subresonance amplitudes in the NMR-ON spectrum, if the subresonance structure is resolved.

TABLE I. Details of the sample preparation.

Experiment	Dimensions[a] (mm)	Surface preparation	E_{impl} (keV)	Number of probe nuclei[b]	Implantation dose[c] ($1/cm^2$)	Annealing
^{183}Os,^{183}Re*Fe*	8×8×0.88	sputter.	60	5×10^{9}	1×10^{11}	1 h at 1070 K
^{191}Pt*Ni*	12×12×0.74	electropol.	60	4×10^{11}	4×10^{12}	no
^{186}Ir*Ni*	12×8×0.85	sputter.	60	2×10^{11}	2×10^{12}	no

[a]Long axis × short axis × thickness of the disk-shaped single crystal.

[b]Estimated via the observed γ activity.

[c]Dimensions (and position) of the beam spot determined by autoradiography.

The sign of the quadrupole splitting cannot be obtained from the MAPON spectrum, since both signs of $\Delta\nu_Q$ are projected onto the positive $\Delta\nu$ axis. However, the final state after the sweep depends on the sweep direction. The respective difference in the relaxation of the γ anisotropy back to equilibrium is very characteristic and can be used to determine the sign of $\Delta\nu_Q$: If the sweep first enters the subresonance between the most occupied sublevels, the relaxation lasts longer and starts with a much broader peak than if it first enters the subresonance between the least occupied sublevels. Examples for this difference, which is referred to in the following as the ''sweep asymmetry,'' will be found in Sec. IV. Either AFP or MAPON sweeps with $\Delta\nu > \Delta\nu_Q$ can be used.[12]

III. EXPERIMENTAL DETAILS

The samples were Fe and Ni single-crystal disks with (110) plane that were spark cut from commercially available bulk single crystals. The orientation of the plane perpendicular to [110] and the marking of the [100] direction within the plane was controlled by Laue backscattering and was accurate within about 0.3°. Table I summarizes the sample dimensions and other important parameters of the sample preparation.

A careful surface preparation proved to be crucial to reduce the inhomogeneous broadening, especially that of the SO-EFG, to a tolerable extent. To remove the structural damage at the surface after the mechanical polishing steps the sample was either electropolished or sputtered by Ar^+ ions. The narrowest EFG distribution was obtained on the electropolished Ni sample, but the sputtering procedure proved to be more reliable and yielded altogether the better results. The sample for the Pt*Ni* experiment was electropolished ≈4 min in H_2SO_4 (66%), a Pt anode was used, and a voltage $U=1.25$ V was applied. The other samples were prepared by repeated cycles of Ar+ ion sputtering (at 300 K) and annealing (at 830 K for Fe and at 870 K for Ni) in a commercial VG ESCALAB 200 UHV chamber. The concentration of impurities at the surface and the ordering of the surface were controlled by x-ray photoelectron spectroscopy and low energy electron diffraction.

The systematic investigation of the SO-EFG was made possible by implantations at the on-line mass separator ISOLDE at CERN. There a long chain of Hg isotopes is available after spallation reactions that are generated by 600 MeV protons in a liquid Pb target. The $5d$ impurities are obtained via the mass separator implantation of a suitable Hg precursor which decays into the desired isotope. Suitable radioactive isotopes are available in this way for the complete upper $5d$ series (Re to Hg) with relatively high yields and virtually no contamination from other masses. At the implantation energy of 60 keV the impurities are distributed in a depth of ≈25 nm below the surface within a layer of ≈15 nm width. This means for the low implantation doses in our experiments (see Table I) that the impurity concentration was always well below 10^{-4}.

It is well known that a heat treatment after the implantation can considerably reduce the linewidths. Previous experiments on Ir*Fe* and Pt*Fe* showed that annealing well over 870 K was necessary to obtain small linewidths. In contrast, no improvement by annealing was found in Ir*Ni* experiments. Therefore, the Fe sample was annealed, the Ni samples not. After the annealing the Fe sample was slowly (within 1 h) cooled down to room temperature.

After the implantation and annealing the samples were soldered with GaIn to a Cu coldfinger and loaded into a ^{3}He-^{4}He dilution refrigerator (model TL-400 from Oxford Instruments). The experiments were performed at temperatures around 10 mK. The γ radiation was detected with four Ge detectors placed at 0°, 90°, 180°, and 270° with respect to the magnetic field that was used to magnetize the sample. The γ anisotropy was measured via the quantity ϵ, which is defined as the following ratio of the individual count rates W:

$$\epsilon = \frac{W(0°)+W(180°)}{W(90°)+W(270°)} - 1.$$

The frequency spectrum for MAPON was generated by mixing the carrier frequency ν_c from a rf synthesizer and $\Delta\nu/2$ from an audio frequency function generator. This produces a spectrum with the two main components at $\upsilon_c + \Delta\nu/2$ and $\upsilon_c - \Delta\nu/2$ and ensures that the separation between these two frequencies remains constant when ν_c is swept over the resonance.[17] The carrier frequency and higher side bands were suppressed with respect to the two main components by more than 25 dB for ^{183}Re*Fe* and by more than 30 dB for the other experiments. The rf power was applied only during the sweep.

The rf signal generators, the timing of the sweep, and the data acquisition were controlled by computer via a CAMAC system. The temperature was determined by a ^{60}Co*Co*(hcp) nuclear orientation thermometer.

The magnetic field was applied along the [100], [110], or [111] direction ([100], [110], or [111] geometry). All three directions lie in the (110) plane of our samples. For each geometry the sample had to be newly mounted on the cold finger and loaded into the refrigerator to place the respective crystallographic direction parallel to the field of the magnet.

A peculiar feature of these three geometries is that a complete orientation of the magnetization along the magnetic field is already obtained at a finite magnetic field strength, which is given by $B_a + B_{\mathrm{dem}}$. The anisotropy fields B_a in the (110) plane are, according to the anisotropy constants from Ref. 29, in Fe, 0.008 T for the [110] geometry and 0.044 T for the [111] geometry, and in Ni, 0.49 T for the [100] geometry and 0.19 T for the [110] geometry. The easy directions for Fe and Ni are [100] and [111], respectively. B_{dem} was of the order of 0.15 T for the ^{183}Os*Fe* and ^{183}Re*Fe* experiment, 0.02 T for the ^{191}Pt*Ni* experiment, and 0.03 T for the ^{186}Ir*Ni* experiment.

The orientation of the magnetization was monitored as a function of the magnetic field via the γ anisotropy. The magnetic and electric hyperfine interactions for $M\|[100]$, $M\|[110]$, and $M\|[111]$ were measured for magnetic fields well above $B_a + B_{\mathrm{dem}}$ to ensure the complete orientation of the magnetization M. The complete orientation was also experimentally tested: The EFG was measured in most cases also for a second, considerably larger field. No change in the EFG with the magnetic field was detected in this way, as is expected for a complete orientation along the direction of the magnetic field.

In the Ni experiments the SO-EFG was also measured in the range $B_{\mathrm{ext}} < B_a + B_{\mathrm{dem}}$. In this range the magnetization rotates from the easy to the hard direction and every orientation of the magnetization in the (110) plane can in principle be realized by an appropriate choice of B_{ext} and the geometry. The only problem is to specify for a given B_{ext} the direction of the magnetization. This direction could be calculated typically within $\pm 5°$. The error comes from (i) the spread of the anisotropy constants in the literature, (ii) a possible misalignment ($\leqslant 2°$) of the sample, and (iii) demagnetization effects in the magnetization behavior, which are difficult to describe exactly.

No measurements in the range $B_{\mathrm{ext}} < B_a + B_{\mathrm{dem}}$ were performed for the Fe sample, because for $B_{\mathrm{dem}} \gg B_a$ the magnetization behavior is dominated by domain growth rather than by rotation of the magnetization, and the direction of the magnetization for a given B_{ext} is difficult to specify.

IV. EXPERIMENTAL RESULTS

A. ^{183}Os*Fe*

Only about 5×10^9 $A = 183$ nuclei could be implanted during 4 h of implantation because of the rapid decline of the Hg yields with decreasing mass number for $A < 185$. Moreover, the half-life of ^{183}Os is only 13 h. Nevertheless, NMR-ON and MAPON measurements could be performed for all three major orientations of the magnetization. The measurements and the deduced hyperfine splitting frequencies are compiled in Table II.

TABLE II. NMR-ON and MAPON results for ^{183}Os*Fe*.

Geometry	B_{ext} (T)	ν_m (MHz)	Γ_m (MHz)	$\Delta\nu_Q^{(0)}$ (MHz)	Γ_Q (MHz)
[100]	0.2	151.45(18)	0.6(7)	+0.283(8)	0.294(23)
	0.4			+0.279(9)	0.297(26)
[110]	0.4	151.36(14)	0.8(4)	+0.208(6)	0.206(17)
	0.6			+0.182(13)	0.251(39)
[111]	0.4	151.41(10)	0.8(1)	+0.187(6)	0.168(13)
	0.6			+0.191(5)	0.165(13)

The NMR-ON spectrum for $M\|[111]$ is shown in Fig. 1. It can be well described by a single Gaussian line. However, if we take the quadrupole splitting into account, we find that the resonance center is shifted with respect to ν_m by $-0.47(10)$ MHz. The linewidth is also in part due to the quadrupole splitting. With $B_{\mathrm{dem}} = 0.16(5)$ T, 0.14(5) T, and 0.15(5) T for $M\|[100]$, $M\|[110]$, and $M\|[111]$, and $d\nu/dB_{\mathrm{ext}} = -1.35(3)$ MHz/T, we obtain, according to Eqs. (5) and (8), the following magnetic hyperfine splittings at zero field:

$$\nu_m^{(0)}(^{183}\mathrm{Os}Fe, M\|[100]) = 151.50(19)\ \mathrm{MHz},$$

$$\nu_m^{(0)}(^{183}\mathrm{Os}Fe, M\|[110]) = 151.71(16)\ \mathrm{MHz},$$

$$\nu_m^{(0)}(^{183}\mathrm{Os}Fe, M\|[111]) = 151.75(12)\ \mathrm{MHz}.$$

These results deviate from $\nu_m^{(0)}(^{183}\mathrm{Os}Fe) = 149.9(2)$ MHz from Ref. 30. The main reason for this deviation is that an erroneous quadrupole splitting was assumed in Ref. 30. For the determination of the g factor, however, this has only minor consequences: With $B_{\mathrm{HF}}(^{189}\mathrm{Os}Fe) = 110.62(2)$ T,[31] $\nu_m^{(0)} = 151.6(3)$ MHz, and the hyperfine anomaly $|^{183}\Delta^{189}| \leqslant 2\%$ we obtain $g(^{183}\mathrm{Os}) = 0.180(4)$ instead of 0.176(3) from Ref. 30.

MAPON spectra for the different orientations of the magnetization are shown in Fig. 2. The frequency was swept, for example, for $M\|[111]$ and $B_{\mathrm{ext}} = 0.4$ T in 1 s from 149 to 154 MHz. For other magnetic fields and/or quadrupole splittings the sweep range was modified accordingly. The distri-

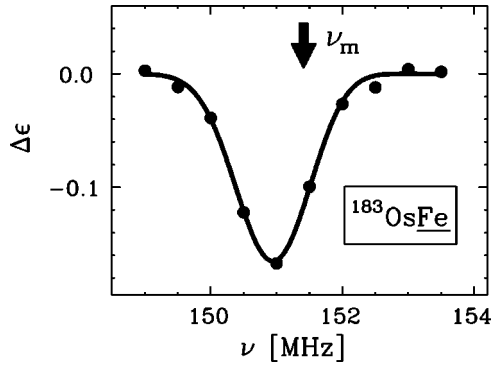

FIG. 1. ^{183}Os*Fe* NMR-ON spectrum for $M\|[111]$ and $B_{\mathrm{ext}} = 0.4$ T. Modulation bandwidth $\Delta\nu^{\mathrm{rf}} = \pm 0.5$ MHz, $T \approx 13$ mK. The arrow marks the position of ν_m.

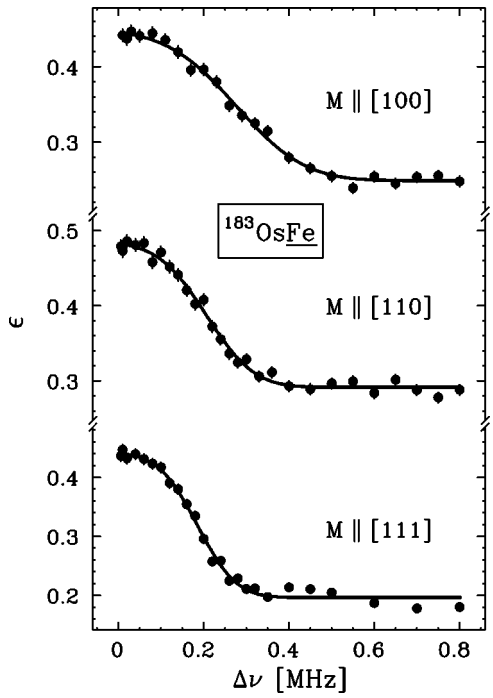

FIG. 2. ^{183}OsFe MAPON spectra for different orientations of the magnetization. B_{ext}=0.4 T.

butions of the quadrupole splitting $P(\Delta\nu_Q)$, deduced by differentiation of the MAPON spectra, are shown in Fig. 3. Table II shows that the quadrupole splittings for different magnetic fields are in perfect agreement apart from

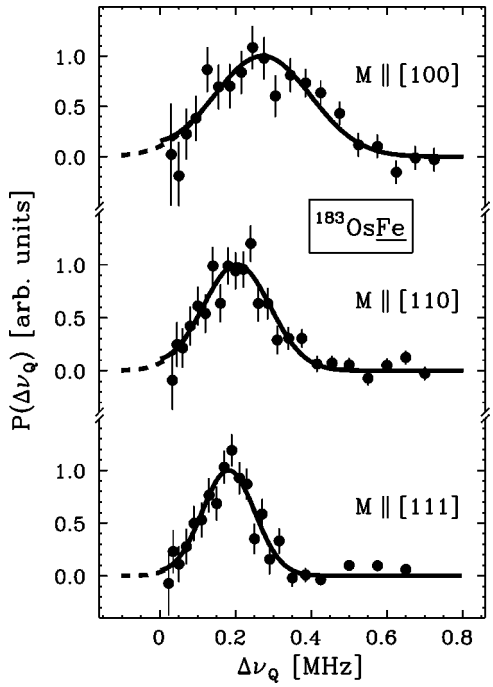

FIG. 3. $P(\Delta\nu_Q)$ of ^{183}OsFe for different orientations of the magnetization, obtained by differentiation of the MAPON spectra in Fig. 2. Due to a small fraction of probe nuclei with negative $\Delta\nu_Q$, the derivative of the MAPON spectrum (solid line and data points) and $P(\Delta\nu_Q)$ (dashed line) are not completely identical.

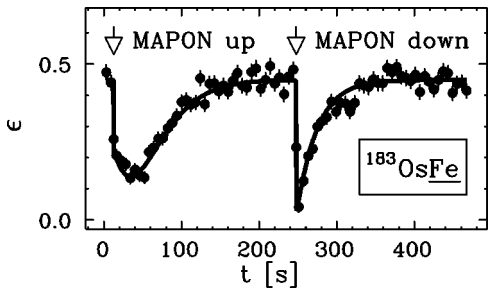

FIG. 4. Asymmetry in the ^{183}OsFe MAPON postpassage signal for $\Delta\nu > \Delta\nu_Q$ in [111] geometry. B_{ext}=0.4 T.

$M\|[110]$, where they differ by two standard deviations. We adopt as the final results

$$\Delta\nu_Q^{(0)}(^{183}\text{Os}Fe, M\|[100]) = +0.281(6)\ \text{MHz},$$

$$\Delta\nu_Q^{(0)}(^{183}\text{Os}Fe, M\|[110]) = +0.203(11)\ \text{MHz},$$

$$\Delta\nu_Q^{(0)}(^{183}\text{Os}Fe, M\|[111]) = +0.189(4)\ \text{MHz}.$$

The sign of the quadrupole splitting was determined from the AFP or MAPON sweep asymmetry. It is positive for all directions of the magnetization. Figure 4 shows the MAPON sweep asymmetry for $M\|[111]$. It also shows that the overall MAPON effect, which was in this case averaged for the MAPON spectrum over a time window of 84 s after the sweep, is slightly larger for sweep up. Therefore, sweep up was used for all MAPON measurements.

B. ^{183}ReFe

After the decay of ^{183}Os the ^{183}OsFe sample was used for a further series of experiments on the daughter isotope ^{183}Re ($I^\pi = 5/2^+, T_{1/2} = 71$ d). Table III compiles the measurements and the deduced hyperfine splitting frequencies. Because of the weak ^{183}Re activity, the resonance was measured only for $M\|[100]$ and $M\|[111]$ and only one MAPON spectrum was measured for each geometry.

Figure 5 shows the NMR-ON spectrum for $M\|[100]$. Again, there is no indication of the quadrupole splitting in the spectrum. Taking into account the quadrupole splitting, the demagnetization fields, and $d\nu/dB_{\text{ext}}(^{183}\text{Re}) = -9.53(10)$ MHz/T we deduce

$$\nu_m^{(0)}(^{183}\text{Re}Fe, M\|[100]) = 724.35(51)\ \text{MHz},$$

$$\nu_m^{(0)}(^{183}\text{Re}Fe, M\|[111]) = 724.71(48)\ \text{MHz}.$$

TABLE III. NMR-ON and MAPON results for ^{183}ReFe.

Geometry	B_{ext} (T)	ν_m (MHz)	Γ_m (MHz)	$\Delta\nu_Q^{(0)}$ (MHz)	Γ_Q (MHz)
[100]	0.2	723.97(18)	2.2(3)	+0.671(20)	0.784(29)
[110]	0.4			+0.606(24)	0.575(69)
[111]	0.4	722.33(14)	2.6(3)	+0.589(10)	0.354(23)

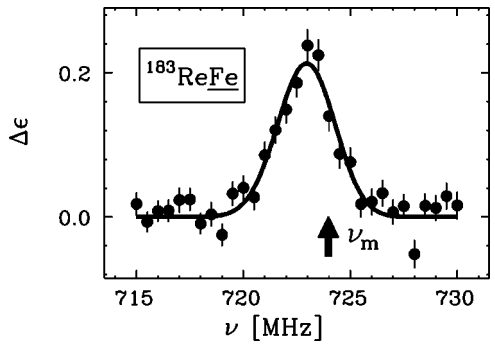

FIG. 5. ^{183}ReFe NMR-ON spectrum for $M\|[100]$ and $B_{\rm ext}=0.2$ T. $\Delta\nu^{\rm rf}=\pm 1.0$ MHz, $T\approx 26$ mK.

In Ref. 32, $\nu_m^{(0)}(^{183}\mathrm{Re}Fe)=722.28(37)$ MHz was reported, about 2 MHz smaller than found in this work. However, the quadrupole splitting, which shifts the resonance center by $-1.0(1)$ MHz in our experiment, is not taken into account in Ref. 32. The remaining difference of about 1 MHz might be ascribed to the structural damage in the samples of Ref. 32, where the resonance linewidth was $\Gamma=5.6$ MHz compared to $\Gamma=2.8$ MHz in our experiment. However, the discrepancy in $\nu_m^{(0)}$ is well below 1% and, therefore, does not affect the derivation of the nuclear g factor of ^{183}Re.

Figures 6 and 7 show the MAPON spectrum and $P(\Delta\nu_Q)$ for [100], [110], and [111] orientations of the magnetization. Care was taken to measure especially the [100] spectrum with high statistics since the precise determination of the center of the MAPON spectrum becomes rapidly more difficult as the inhomogeneous broadening exceeds 100%. The choice of the sweep time and the rf power required also some

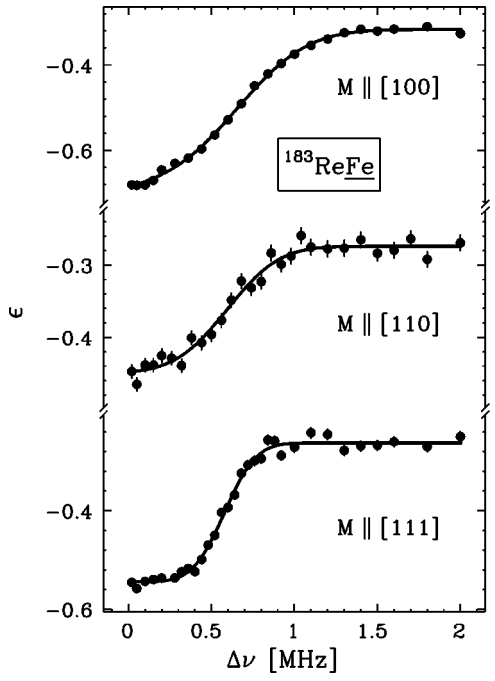

FIG. 6. ^{183}ReFe MAPON spectra for different orientations of the magnetization. $B_{\rm ext}=0.2$ T ([100] geometry) or $=0.4$ T ([110] and [111] geometry).

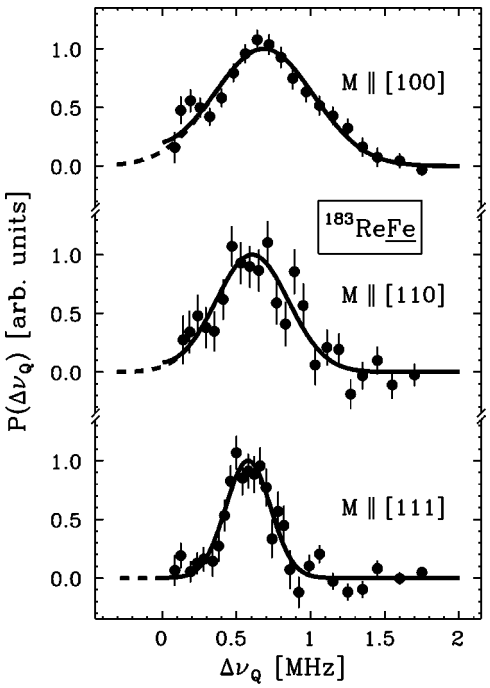

FIG. 7. $P(\Delta\nu_Q)$ of ^{183}ReFe, deduced from the MAPON spectra in Fig. 6.

care to minimize both the nuclear spin-lattice relaxation during the sweep and the power broadening. For example, the carrier frequency was swept in [100] geometry from 718.5 MHz to 729.5 MHz in 0.1 s. The shift of the center of the MAPON spectrum relative to $\Delta\nu_Q^{(0)}$ was estimated in this case as $-7(7)$ and $-9(8)$ kHz due to the power broadening and the relaxation during the sweep, respectively. The results in Table III are already corrected for these effects.

The sign of the quadrupole splitting was determined from the characteristic form of the postpassage signal after the MAPON sweep for sweep up and $\Delta\nu>\Delta\nu_Q^{(0)}$. It is positive for all orientations of the magnetization. The positive sign was confirmed in [100] geometry by an AFP measurement, which is shown in Fig. 8.

C. ^{191}PtNi

The hyperfine interaction of ^{191}PtNi was investigated for the first time. The hyperfine field of PtNi had already been

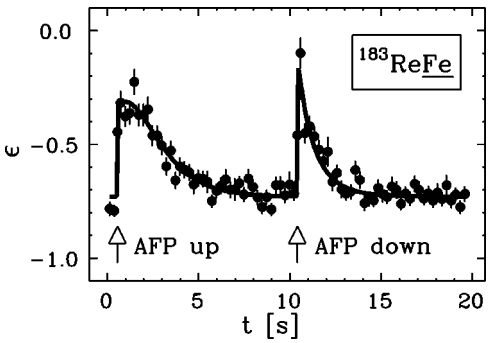

FIG. 8. ^{183}ReFe postpassage signal after AFP sweep up and down. [100] geometry, $B_{\rm ext}=0.2$ T.

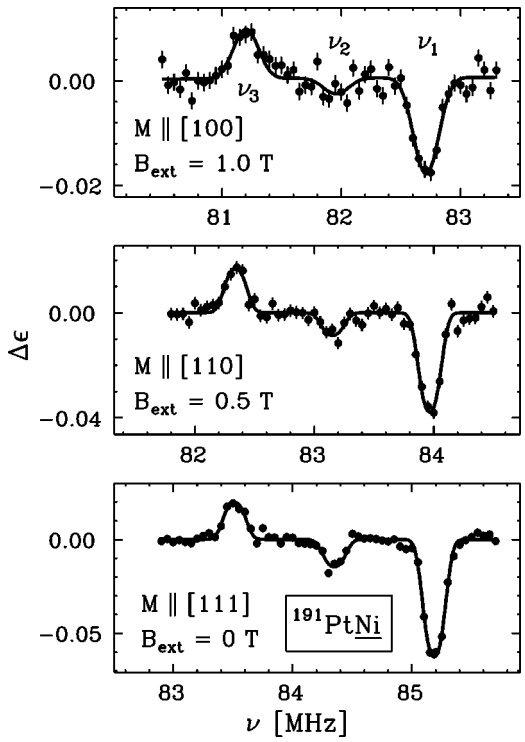

FIG. 9. ^{191}Pt*Ni* NMR-ON spectra for different orientations of the magnetization. $\Delta\nu^{\mathrm{rf}}=\pm 0.1$ MHz. The frequency axes are shifted relative to each other by $-(d\nu/dB_{\mathrm{ext}})(B_{\mathrm{ext}}-B_{\mathrm{dem}})$ so that the positions of the resonances can be directly compared.

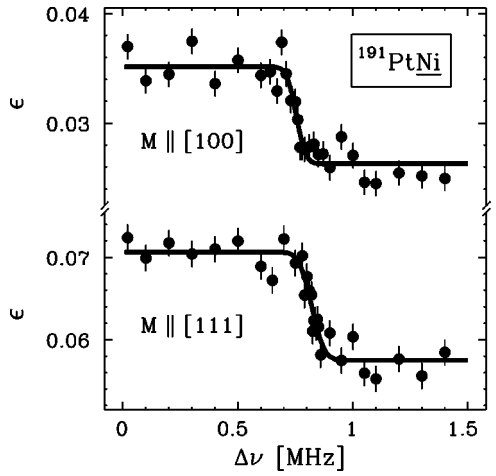

FIG. 10. ^{191}Pt*Ni* MAPON spectra for [100] geometry and $B_{\mathrm{ext}}=0.6$ T (top) and for [111] geometry and $B_{\mathrm{ext}}=0$ (bottom).

determined with spin-echo NMR on stable ^{195}Pt,[33] but no investigation of the SO-EFG was possible because $I(^{195}\mathrm{Pt})=1/2$.

NMR-ON spectra for $M\|[100]$, $M\|[110]$, and $M\|[111]$ are shown in Fig. 9. In contrast to the situation for most $5d$ impurities in Fe and Ni, the subresonance structure is clearly resolved and $\Delta\nu_Q^{(0)}$ can be determined by NMR-ON. The arrangement of the subresonance amplitudes directly gives the sign of the quadrupole splitting. It is negative for all orientations of the magnetization. NMR-ON turned out to be even more efficient for the determination of $\Delta\nu_Q^{(0)}$ than MAPON. Therefore, only two MAPON measurements were performed. The MAPON sweep range was very large compared to the NMR-ON modulation bandwidths of ± 0.1 or ± 0.15 MHz: For example, the carrier frequency was swept for the [111] spectrum from 86.1 to 82.1 MHz in 1 s. The MAPON spectra are shown in Fig. 10. The sharp transitions from $\Delta\nu<\Delta\nu_Q$ to $\Delta\nu>\Delta\nu_Q$ indicate an unusually small inhomogeneous broadening of the SO-EFG of only about 10%, the smallest so far observed in cubic Fe, Co, and Ni.

The MAPON and NMR-ON results for $M\|[100]$, $M\|[110]$, and $M\|[111]$ are listed in Table IV. With $d\nu/dB_{\mathrm{ext}}$ and B_{dem} as deduced below, we obtain for the magnetic hyperfine splitting

$$\nu_m^{(0)}(^{191}\mathrm{Pt}Ni, M\|[100])=84.346(45)\ \ \mathrm{MHz},$$

$$\nu_m^{(0)}(^{191}\mathrm{Pt}Ni, M\|[110])=84.320(44)\ \ \mathrm{MHz},$$

$$\nu_m^{(0)}(^{191}\mathrm{Pt}Ni, M\|[111])=84.349(4)\ \ \mathrm{MHz}.$$

Table IV shows that for each geometry the quadrupole splittings for different magnetic fields and from the NMR-ON and MAPON measurements are in reasonable agreement. By combining all results we obtain

$$\Delta\nu_Q^{(0)}(^{191}\mathrm{Pt}Ni, M\|[100])=-0.757(5)\ \ \mathrm{MHz},$$

$$\Delta\nu_Q^{(0)}(^{191}\mathrm{Pt}Ni, M\|[110])=-0.814(5)\ \ \mathrm{MHz},$$

$$\Delta\nu_Q^{(0)}(^{191}\mathrm{Pt}Ni, M\|[111])=-0.833(6)\ \ \mathrm{MHz}.$$

In [100] and [110] geometries additional NMR-ON measurements were performed in the range $B_{\mathrm{ext}}<B_a$. The re-

TABLE IV. NMR-ON and MAPON results for ^{191}Pt*Ni* in the range $B_{\mathrm{ext}}>(B_a+B_{\mathrm{dem}})$.

Geometry	B_{ext} (T)	ν_m (MHz)	Γ (MHz)	$\Delta\nu_Q^{(0)}$ (NMR-ON) (MHz)	$\Delta\nu_Q^{(0)}$ (MAPON) (MHz)	Γ_Q (MHz)
[100]	0.6	82.934(12)	0.15(5)	−0.769(11)	−0.753(8)	0.08(3)
	1.0	81.956(9)	0.20(2)	−0.755(9)		
[110]	0.3	83.651(10)	0.22(3)	−0.814(11)		
	0.5	83.152(5)	0.11(2)	−0.814(5)		
[111]	0.0	84.349(4)	0.11(1)	−0.837(4)	−0.821(6)	0.10(2)
	0.1	84.104(12)	0.17(3)	−0.838(12)		

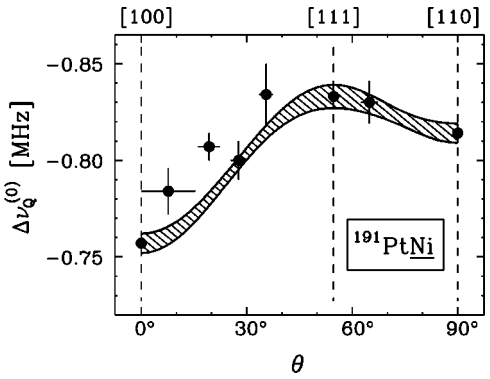

FIG. 11. Angular dependence of the ^{191}Pt*Ni* quadrupole splitting in the (110) plane. θ is the angle of the magnetization in the (110) plane relative to the [100] axis (θ=0° for $M\|[100]$, =54.7° for $M\|[111]$, =90° for $M\|[110]$). The data at θ=8°, 19°, 28°, 36°, and 65° were measured in [100] geometry at $B_{\rm ext}$=0.5, 0.4, 0.3, and 0.2 T and in [110] geometry at $B_{\rm ext}$=0.1 T, respectively. The hatched band is the extrapolation of $\Delta\nu_Q^{(0)}([100])$, $\Delta\nu_Q^{(0)}([110])$, and $\Delta\nu_Q^{(0)}([111])$ according to Eq. (13).

spective $\Delta\nu_Q^{(0)}$'s are shown in Fig. 11 as a function of the direction of the magnetization in the (110) plane. As expected, all $\Delta\nu_Q^{(0)}$'s are somewhere between the maxima and minima at $M\|[111]$ and $M\|[100]$. However, the limited accuracy and the small anisotropy of the SO-EFG allow no further conclusions on the form of the anisotropy.

The resonance shift with the magnetic field was investigated in the [111] geometry by NMR-ON measurements of the ν_1 resonance. Table V presents the respective data. It can be perfectly described by Eqs. (5) and (8) using the following parameters:

$$d\nu/dB_{\rm ext} = -2.449(8)\ \ \text{MHz/T},$$

$$B_{\rm dem}([111]) = 0.0094(15)\ \ \text{T}.$$

The result for $B_{\rm dem}$ is significantly "too small": The minimum demagnetization field in the center of the sample is calculated to be 0.020 T; the effective average $B_{\rm dem}$ for the beam spot should be around 0.025 T. We have found no explanation for this discrepancy. To deduce $\nu_m^{(0)}$ for the other orientations of the magnetization we adopted $B_{\rm dem}$=0.017(10) T. $d\nu/dB_{\rm ext}$ is in perfect agreement

TABLE V. ^{191}Pt*Ni*: shift of the ν_1 resonance with $B_{\rm ext}$.

Geometry	$B_{\rm ext}$ (T)	ν_1 (MHz)
[111]	0.0	85.185(2)
	0.008	85.183(7)
	0.015	85.169(4)
	0.1	84.966(5)
	0.5	83.984(5)
	1.0	82.757(8)

TABLE VI. ^{191}Pt*Ni*: calculated and measured subresonance amplitude ratios for the three NMR-ON spectra in Fig. 9.

Geometry	T (mK)	Calculated I_2/I_1	Calculated I_3/I_1	Experiment I_2/I_1	Experiment I_3/I_1
[100]	17.6	0.17	−0.55	0.13(6)	−0.56(7)
[110]	13.9	0.20	−0.47	0.23(4)	−0.44(5)
[111]	9.8	0.24	−0.33	0.23(2)	−0.32(3)

with −2.47(4) MHz/T, which is expected from $g(^{191}\text{Pt}) = 0.329(5)$ (Ref. 34) if the diamagnetic shielding is taken into account.

The clear separation of the subresonances offered also the rare opportunity to test our calculation of the subresonance amplitudes, which is else used to deduce ν_m from unresolved subresonance structures. Table VI compares the calculated amplitude ratio I_i/I_1 of the ith subresonance to the ν_1 resonance with the observed ratio. The calculated and experimental amplitudes are found to be in perfect agreement.

D. ^{186}Ir*Ni*

The quadrupole splitting of the Ir*Ni* NMR spectrum was resolved in the past for ^{194}Ir, ^{193}Ir, ^{192}Ir, ^{191}Ir, and ^{188}Ir. This was so far not possible for ^{186}Ir, because the ratio $\Delta\nu_Q/\Gamma_m \propto Q/[gI(2I-1)]$ is considerably smaller for this isotope. However, due to the MAPON technique, this represents no longer a problem. Therefore, we chose ^{186}Ir as the

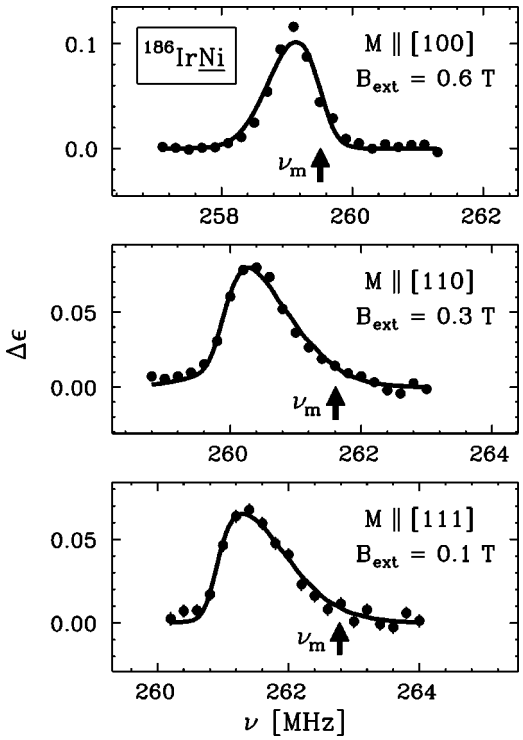

FIG. 12. ^{186}Ir*Ni* NMR-ON spectra for different orientations of the magnetization. $\Delta\nu^{\rm rf}=\pm 0.2$ MHz, $T\approx 25$ mK for $M\|[100]$ and ≈ 20 mK for $M\|[110]$ and $M\|[111]$. The frequency axes are displaced relative to each other by $-(d\nu/dB_{\rm ext})(B_{\rm ext}-B_{\rm dem})$ to compensate the different magnetic fields.

TABLE VII. NMR-ON and MAPON results for ^{186}Ir*Ni* in the range $B_{\rm ext} > (B_a + B_{\rm dem})$.

Geometry	$B_{\rm ext}$ (T)	ν_m (MHz)	Γ_m (MHz)	$\Delta\nu_Q^{(0)}$ (MHz)	Γ_Q (MHz)
[100]	0.6	259.51(10)	0.17(23)	+0.157(5)	0.202(13)
	0.8			+0.160(5)	0.186(13)
[110]	0.3	261.61(12)	0.27(10)	+0.351(3)	0.107(8)
	0.4			+0.348(2)	0.103(6)
	0.7			+0.344(3)	0.123(9)
[111]	0.1	262.78(13)	0.29(10)	+0.3744(15)	0.060(4)
	0.3			+0.3723(21)	0.075(7)

probe isotope, since it combines strong γ transitions, large γ anisotropies, and a convenient resonance frequency in Ni.

The ^{186}Ir resonance was measured for $M\|[100]$, $M\|[110]$, and $M\|[111]$. Figure 12 shows the NMR-ON spectra. The deduced magnetic hyperfine splittings are listed in Table VII. With $d\nu/dB_{\rm ext} = -5.78(6)$ MHz/T and $B_{\rm dem} = 0.017(6)$ T, 0.040(13) T, and 0.032(11) T for the [100], [110], and [111] geometries, we finally derive

$$\nu_m^{(0)}(^{186}\mathrm{Ir}Ni, M\|[100]) = 262.88(11)\ \text{MHz},$$

$$\nu_m^{(0)}(^{186}\mathrm{Ir}Ni, M\|[110]) = 263.11(14)\ \text{MHz},$$

$$\nu_m^{(0)}(^{186}\mathrm{Ir}Ni, M\|[111]) = 263.17(14)\ \text{MHz}.$$

These results are in agreement with $\nu_m^{(0)}(^{186}\mathrm{Ir}Ni) = 263.17(8)$ MHz from Ref. 35.

The subresonance amplitudes, which are needed to describe the form of the NMR-ON spectrum, were calculated assuming $U_2A_2 = -0.31$ and $U_4A_4 = -0.14$ for the angular distribution coefficients of the 297 keV transition of ^{186}Ir. These coefficients were determined in a recent ^{186}Ir*Fe* experiment,[36] and they are given here since no explicit values are available in the literature, although several nuclear orientation experiments on ^{186}Ir had been reported.

Although the quadrupole splitting is not resolved in the NMR-ON spectra, it causes an asymmetric shape of the resonance and a significant displacement of the resonance center relative to ν_m. The strong dependence of the quadrupole splitting on the direction of the magnetization (see below) leads, therefore, also to a distinct change in the position and the shape of the resonance from $M\|[100]$ to $M\|[111]$. This

TABLE VIII. ^{186}Ir*Ni* quadrupole splittings in the range $B_{\rm ext} < (B_a + B_{\rm dem})$.

Geometry	$B_{\rm ext}$ (T)	$\Delta\nu_Q^{(0)}$ (MHz)	Geometry	$B_{\rm ext}$ (T)	$\Delta\nu_Q^{(0)}$ (MHz)
[100]	0.1	+0.353(9)	[110]	0.0	+0.372(3)
	0.2	+0.311(5)		0.05	+0.371(3)
	0.3	+0.255(5)		0.1	+0.365(3)
	0.4	+0.216(5)		0.15	+0.355(5)
	0.5	+0.174(5)		0.2	+0.347(5)

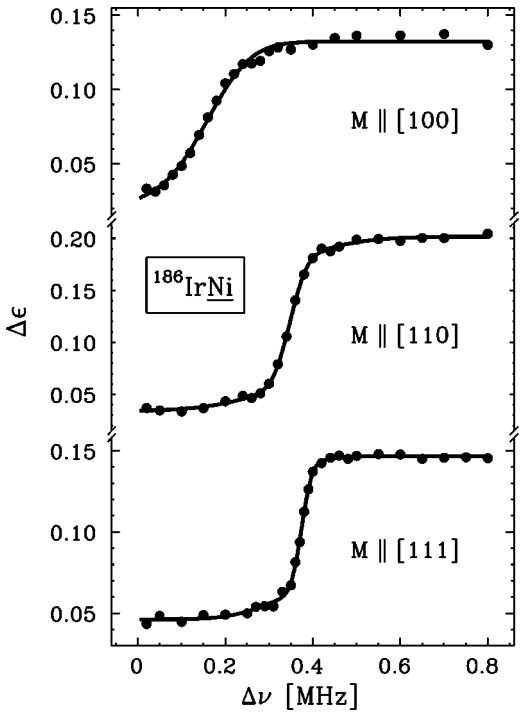

FIG. 13. ^{186}Ir*Ni* MAPON spectra for different orientations of the magnetization. $B_{\rm ext} = 0.8$ T for $M\|[100]$, $= 0.4$ T for $M\|[110]$, and $= 0.1$ T for $M\|[111]$.

effect is clearly visible in Fig. 12. This is in contrast to the NMR-ON results on ^{192}Ir*Ni* in single-crystal samples from Ref. 2. There the quadrupole splitting was deduced from the asymmetric shape of the resonance and no significant change in the center and shape of the resonance was found between $M\|[100]$ and $M\|[111]$. However, the reported quadrupole splitting was also much larger than found in later ^{192}Ir*Ni* experiments.[21,37] This suggests that the asymmetric shape of the ^{192}Ir resonance in Ref. 2 was not due to a quadrupole splitting at all.

For the precise determination of the quadrupole splitting MAPON measurements were performed. The geometries, magnetic fields, and the deduced quadrupole splittings are compiled in Tables VII and VIII. Because of the relatively fast nuclear spin-lattice relaxation, short sweep times were necessary. For example, for the [111] spectrum at $B_{\rm ext} = 0.1$ T the carrier frequency was swept from 260.1 to 266.3 MHz in 0.1 s. However, the shift of the center of the MAPON spectrum due to the power broadening and the relaxation during the MAPON sweep could be kept to below 2 kHz in nearly all cases by a careful choice of the sweep time and the rf power.

MAPON spectra for $M\|[100]$, $M\|[110]$, and $M\|[111]$ are shown in Fig. 13; the respective $P(\Delta\nu_Q)$'s are shown in Fig. 14. The anisotropy of the inhomogeneous broadening of the EFG becomes particularly obvious from these data since it shows the opposite sign as the anisotropy of the SO-EFG. This leads to the conspicuous decrease of the relative width of $P(\Delta\nu_Q)$ from 125% for $M\|[100]$ to 31% for $M\|[110]$ and to 17% for $M\|[111]$.

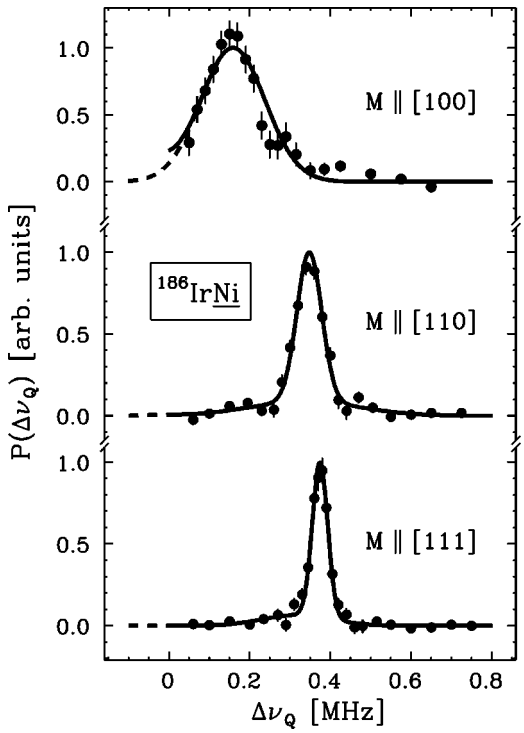

FIG. 14. $P(\Delta\nu_Q)$ of ^{186}IrNi, deduced from the MAPON spectra in Fig. 13.

For each geometry the MAPON measurements at different magnetic fields gave consistent results. We adopt as the final results

$$\Delta\nu_Q^{(0)}(^{186}\mathrm{Ir}Ni, M\|[100]) = +0.1590(46)\ \mathrm{MHz},$$

$$\Delta\nu_Q^{(0)}(^{186}\mathrm{Ir}Ni, M\|[110]) = +0.3470(17)\ \mathrm{MHz},$$

$$\Delta\nu_Q^{(0)}(^{186}\mathrm{Ir}Ni, M\|[111]) = +0.3737(12)\ \mathrm{MHz}.$$

The positive sign of the quadrupole splitting was already known from previous experiments.[35] The characteristic form of the postpassage signal after MAPON sweep up confirmed this sign for all orientations of the magnetization. Figure 15 shows an example.

The quadrupole splitting for other orientations of the magnetization can be deduced from the MAPON data in the

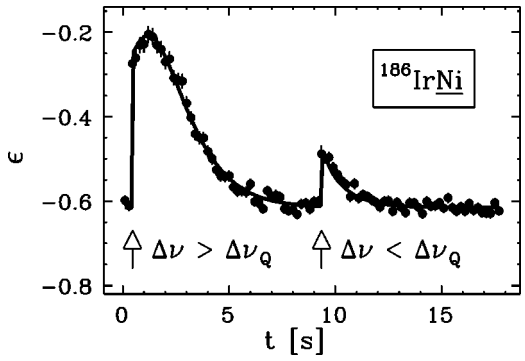

FIG. 15. ^{186}IrNi postpassage signal after MAPON sweep down for $\Delta\nu > \Delta\nu_Q$ and $\Delta\nu < \Delta\nu_Q$. [111] geometry, B_{ext}=0.1 T.

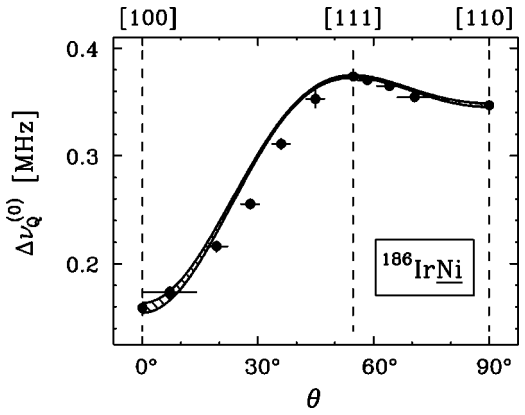

FIG. 16. Angular dependence of the ^{186}IrNi quadrupole splitting in the (110) plane. θ and the hatched band have the same meaning as in Fig. 11.

range $B_{\mathrm{ext}} < B_a$. The complete angular dependence of $\Delta\nu_Q^{(0)}$ in the (110) plane is shown in Fig. 16. As expected, we find a smooth variation of $\Delta\nu_Q^{(0)}$ between [100], [110], and [111]. Figure 16 shows also the lowest-order interpolation of the [100], [110], and [111] data. The experimentally observed form of the anisotropy deviates slightly from this prediction.

The experiment just described was actually already our second ^{186}IrNi experiment (sample II). The first experiment (sample I) was mainly used to optimize the annealing procedure after the implantation. Sample I was annealed after implantation at 940 K and in further steps at 1070 K and 1370 K. After each step the linewidths were measured in [111] geometry by NMR-ON and MAPON. The results are compiled in Table IX together with the respective results for sample II. The fact that the linewidths were considerably larger in sample I than in sample II is not necessarily an effect of the annealing since the surface of sample I was prepared by electropolishing and the surface of sample II by Ar^+ ion sputtering. More relevant is that the already relatively broad linewidths of sample I were increased rather than reduced by the further annealing. This suggested that, in contrast to the experience for Fe, annealing after the implantation is not necessary for the Ni samples. This conclusion was confirmed by the relatively small linewidths in the experiments on sample II and the ^{191}PtNi sample, which both had been not annealed.

The data from Table IX show also the influence of the inhomogeneous broadening on the hyperfine splitting. This

TABLE IX. Center and inhomogeneous broadening of the ^{186}IrNi hyperfine splitting for different samples and heat treatments. All measurements were performed in [111] geometry at B_{ext}=0.1 T.

Sample	Annealing	$\overline{\nu}$ (MHz)	Γ (MHz)	$\Delta\nu_Q^{(0)}$ (MHz)	Γ_Q (MHz)
II	no	261.54(3)	1.2(1)	+0.374(1)	0.06(1)
I	1 h at 940 K	260.08(18)	4.8(4)	+0.370(12)	0.39(4)
	1 h at 1070 K	259.30(16)	5.9(4)	+0.366(12)	0.47(4)
	1 h at 1370 K			+0.384(31)	0.55(11)

TABLE X. SO-EFG in cubic Fe and Ni.

System	$V_{z'z'}$ (10^{16} V/cm^2) $M\|[100]$	$M\|[110]$	$M\|[111]$	Ref.
Au*Fe*	−1.57(7)	−1.03(4)	−0.79(6)	28
Pt*Fe*	−0.12(4)	−0.29(2)	−0.35(2)	23
Ir*Fe*	−4.02(5)	−2.57(6)	−2.17(3)	a
Os*Fe*	+0.89(8)	+0.65(7)	+0.60(5)	b
Re*Fe*	+0.88(9)	+0.79(9)	+0.77(8)	b
Au*Ni*	+0.10(4)	0.00(7)	−0.03(2)	40
Pt*Ni*	+0.72(3)	+0.77(4)	+0.79(4)	b
Ir*Ni*	−0.77(2)	−1.69(2)	−1.82(2)	b
Co*Fe*	+0.29(6)			c
Ni*Ni*			0.07(1)[d]	10

[a]Weighted average for ^{188}Ir*Fe* and ^{189}Ir*Fe* from Refs. 22 and 36.
[b]This work.
[c]Weighted average for ^{57}Co*Fe*, ^{58}Co*Fe*, and ^{60}Co*Fe* from Refs. 17 and 18.
[d]Sign unknown.

information is particularly important for the quadrupole splitting: Since its inhomogeneous broadening is very large on a relative scale, the question arises whether the center of $P(\Delta\nu_Q)$ still represents the intrinsic quadrupole splitting. There exists no experience on this subject, since the precise determination of both $\Delta\nu_Q^{(0)}$ and Γ_Q by the MAPON technique is a rather new achievement. The data from Table IX show that the variation in the width of $P(\Delta\nu_Q)$ from 17% to 140% has no significant influence on the center of $P(\Delta\nu_Q)$. This confirms the interpretation of this center as the intrinsic quadrupole splitting even for large inhomogeneous broadenings. We also note a small but significant shift of the center of the magnetic resonance to lower frequencies with increasing width of the resonance. Similar shifts are well known from NMR experiments in Fe and Ni when the linewidth exceeds 1%.

V. DISCUSSION

A. SO-EFG data

Table X compiles the available data on the SO-EFG in cubic Fe, Co, and Ni for [100], [110], and [111] orientations of the magnetization. The following quadrupole moments were used to obtain the EFG's from the quadrupole splittings of this work: $Q(^{191}\mathrm{Pt}) = -0.87(4)$ b,[34] $Q(^{186}\mathrm{Ir}) = -2.548(31)$ b,[38] $Q(^{183}\mathrm{Os}) = +3.12(27)$ b,[39] and $Q(^{183}\mathrm{Re}) = +2.1(2)$ b.[39] The Au*Fe* data are preliminary, since the surface of the used sample was only mechanically polished and the linewidths were accordingly rather large. A confirmation by an experiment on a more carefully prepared sample would be desirable. The table includes also data from a recent Au*Ni* experiment that will be described elsewhere.[40]

For some systems data are only available from experiments on polycrystalline samples. Table XI summarizes these data. The center of the EFG distribution is in this case only an average, $\langle V_{z'z'}\rangle$, over many different orientations of the magnetization relative to the crystallographic axes. The simplest assumption—that all orientations contribute with equal weight to $\langle V_{z'z'}\rangle$—is not necessarily fulfilled since it requires that the sample be fully magnetized, that there be no textures in the sample, and that the effective rf coupling to the probe nuclei be identical for all orientations. It should be a good approximation for the Co(fcc) data, since the nearly complete absence of textures in the Co(fcc) samples was confirmed by x-ray diffraction. However, no information on textures is available for the Fe*Fe* experiment.

TABLE XI. Average SO-EFG in polycrystalline samples.

System	$\langle V_{z'z'}\rangle$ (10^{16} V/cm^2)	Ref.	System	$\langle V_{z'z'}\rangle$ (10^{16} V/cm^2)	Ref.
Pt*Co*(fcc)	+0.23(5)	24	Re*Co*(fcc)	+0.36(26)	24
Ir*Co*(fcc)	−1.04(5)	24	Fe*Fe*	+0.13(4) [a]	4
Os*Co*(fcc)	−1.15(11)	24			

[a]$T = 299$ K, $Q(^{57}\mathrm{Fe}) = 0.16(1)$ b (Ref. 41).

Precise data on the SO-EFG of the light impurities $(3d, 4d, 5sp, \ldots)$ are still very rare despite MAPON experiments on several of these systems. The reason is the large inhomogeneous broadening of the SO-EFG of considerably more than 100% that was found in all these experiments, with the exception of Co*Fe* in [100] geometry. The MAPON technique allows us to deduce only the upper and lower limits for $\Delta\nu_Q^{(0)}$ from these extremely broadened MAPON spectra.[24] The upper limit is of the same order as the broadening, the lower limit often much smaller.

The upper limit for the SO-EFG that can be deduced from the available MAPON data is for most light impurities of the order of several 10^{15} V/cm^2. The lower limit is of the order of several 10^{14} V/cm^2. Since a table of rather unspecific upper and lower limits would provide only little information on the systematics, we list in Table XII only the sign of the SO-EFG for the light impurities. In most cases it can be unambiguously determined by the sweep asymmetry.

It should be mentioned that rather precise quadrupole splittings were deduced in the past from extremely broad MAPON spectra using a questionable differentiation procedure.[13–16,42] $\Delta\nu_Q^{(0)}$ was determined in these cases as the position of the maximum in the derivative of the MAPON spectrum. The inspection of the MAPON data shows, however, that this maximum is only present in the used derivative. It is either clearly absent or not significant in the slope of the original MAPON spectrum or it is due to the power broadening in the region $\Delta\nu \to 0$. Thus, the deduced maximum of the EFG distribution is in these cases an artifact of the differentiation and/or the power broadening. The quadru-

TABLE XII. Sign of the SO-EFG for $4d$ and $3d$ impurities in cubic Fe, Co, and Ni.

System	sgn($V_{z'z'}$)	Ref.	System	sgn($V_{z'z'}$)	Ref.
Ru*Fe*	−	28	Co*Co*(fcc)	−	42
Zr*Fe*	+	28	Co*Ni*	−	16
Mn*Fe*	−	15	Mn*Ni*	+	13

TABLE XIII. ξ and $\langle 1/r^3\rangle$ for the free atom from Ref. 44 and $\langle l_{z'}^2 - l(l+1)/3\rangle / V_{z'z'}$ for several d elements. a_B is the Bohr radius.

Element	ξ (eV)	$\langle 1/r^3\rangle$ (a_B^{-3})	$\left\langle l_{z'}^2 - \frac{l(l+1)}{3}\right\rangle \Big/ V_{z'z'}$ $[(10^{16}\ \mathrm{V/cm^2})^{-1}]$
Au	0.63	13.3	2.7×10^{-3}
Pt	0.56	11.9	3.0×10^{-3}
Ir	0.48	10.5	3.4×10^{-3}
Os	0.42	9.3	3.9×10^{-3}
Re	0.36	8.1	4.4×10^{-3}
Ni	0.086	7.0	5.2×10^{-3}
Co	0.068	5.9	6.1×10^{-3}
Fe	0.054	5.0	7.2×10^{-3}

pole splittings and EFG's for the light impurities that are compiled, for example, in Refs. 16 or 43 were deduced in this way and are not considered in this work (with the exception of Co*Fe* in [100] geometry).

B. Magnitude of the noncubic charge distribution

The EFG and the charge distribution $e\rho(\vec{r})$ around the nucleus are related by

$$V_{z'z'} = -2e\int \frac{P_2(\cos\vartheta)}{r^3}\rho(\vec{r})d^3r, \tag{9}$$

where ϑ is the angle between $\vec{r}$ and the z' direction. Due to the weighting by r^{-3}, the main contribution comes from the electrons at the lattice site of the probe nucleus. Their noncubic spatial distribution can be expressed in terms of the orbital quantum numbers by the expectation value $\langle l_{z'}^2 - l(l+1)/3\rangle$, which is summed over all occupied states at the impurity site. Assuming that only d electrons are relevant, the following relation to the EFG can be derived from Eq. (9) (Ref. 6):

$$V_{z'z'} = e(2/7)\left\langle l_{z'}^2 - \frac{l(l+1)}{3}\right\rangle \langle 1/r^3\rangle. \tag{10}$$

For p electrons instead of d electrons the prefactor would be 6/5 instead of 2/7. Table XIII lists $\langle 1/r^3\rangle$ and the respective conversion factors between EFG and noncubic charge distribution for several $5d$ and $3d$ elements. Of course, these numbers can serve only as a guide, since they were taken from Hartree-Fock calculations for the free atom. $\langle 1/r^3\rangle$ can deviate in solids considerably from the free atom value, depends on the electron energy, and can in principle be also different for e_g and t_{2g} orbitals.[45]

Taking the conversion factors from Table XIII, we can now deduce the magnitude of the noncubic charge distribution from our data: (i) For the majority of the $5d$ impurities the SO-EFG strength is near 1×10^{16} V/cm^2 and $|\langle l_{z'}^2 - l(l+1)/3\rangle|$ ranges between 2.1×10^{-3} and 4.5×10^{-3}. (ii) Considerably larger $\langle l_{z'}^2 - l(l+1)/3\rangle$'s are found only for Ir*Fe*(13.7×10^{-3} for $M\|[100]$ and 7.4×10^{-3} for $M\|[111]$) and Ir*Ni* (6.2×10^{-3} for $M\|[111]$). It is thus not accidental that the SO-EFG was first found for these systems. (iii) $\langle l_{z'}^2 - l(l+1)/3\rangle$ can also be about an order of magnitude smaller: This is the case for Pt*Fe* (0.4×10^{-3} for $M\|[111]$), Pt*Co*(fcc) (0.7×10^{-3}), and Au*Ni* (0.2×10^{-3}).

The magnitude of the noncubic charge distribution is else only known for the $3d$ systems Ni*Ni*($M\|[111]$), Co*Fe*($M\|[100]$), and Fe*Fe*: $|\langle l_{z'}^2 - l(l+1)/3\rangle| \approx 0.4\times10^{-3}$, 1.8×10^{-3}, and 0.9×10^{-3}, respectively. It is difficult to decide at the moment whether these numbers are typical for the $3d$ impurities or represent only a selection of the very largest noncubic charge distributions.

The magnitude of the noncubic charge distribution reflects the quenching of spin-orbit effects in transition metals: The mixing of states by the SOC is suppressed by the energy splitting of these states within the band structure. The noncubic charge distribution appears in a perturbative treatment of the SOC in second order. Therefore, it scales with $(\xi/W)^2$. ξ is here the SOC strength, defined by the expression $\xi\vec{s}\vec{l}$ for the SOC; W is the bandwidth. Table XIII lists ξ for several transition-metal elements. Again, these numbers can serve only as a guide since they were calculated for the free atom.

The prefactor in front of $(\xi/W)^2$ depends on the band structure in the particular case. Its general order of magnitude is investigated in part II: For a band with uniform spin direction and smooth density of states $|\langle l_{z'}^2 - l(l+1)/3\rangle|$ is somewhere between 0 and 10 $(\xi/W)^2$. However, the structure of the band and the overlap of spin-up and spin-down bands also play a role. The model calculations on more realistic band structures indicate that $\langle l_{z'}^2 - l(l+1)/3\rangle$ ranges up to about 14 $(\xi/W)^2$ for an Fe-like band structure and up to about 5 $(\xi/W)^2$ for local band structures similar to those of Re, Os, or Ir in Fe. Taking $W\approx5.5$ eV, $\xi(5d)\approx0.5$ eV, and $\xi(3d)\approx0.07$ eV we expect accordingly noncubic charge distributions up to 40×10^{-3} for the $5d$ elements and up to 2.3×10^{-3} for the $3d$ elements.

The few data on the $3d$ elements are in in full accord with this rough estimate. However, the noncubic charge distributions of the $5d$ impurities are all smaller than a third of what in principle should be possible for these systems. This may point to an additional suppression of the SOC for these systems, but may also be accidental. Moreover, our estimates are based on free atom values for $\langle 1/r^3\rangle$ and ξ and on model band structures. More accurate calculations will be necessary to see if the theory really overestimates the magnitude of the effect.

The observation of several particularly small noncubic charge distributions can be explained by the strong variation of the effect with the impurity (see below): Since there are several sign changes in the systematics, some systems accidentally lie close to a sign change.

C. Systematics of the noncubic charge distribution

The SO-EFG of the $5d$ impurities in cubic Fe, Co, and Ni is shown in Fig. 17 as a function of the atomic number of the

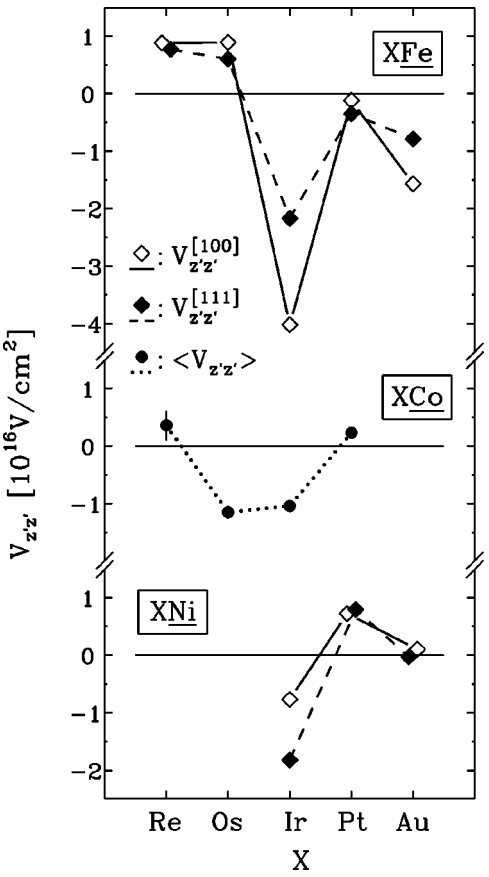

FIG. 17. SO-EFG of the $5d$ impurities in cubic Fe, Co, and Ni. If data from single-crystal samples are available, $V^{[100]}_{z'z'}$ (open diamonds) and $V^{[111]}_{z'z'}$ (solid diamonds) is shown. Otherwise, only an average EFG $\langle V_{z'z'}\rangle$ (solid circles) is shown.

impurity. Positive SO-EFG's correspond to oblate deformations of the electron distribution (oblate with respect to the direction of the magnetization), negative SO-EFG's to prolate deformations.

The parameters ξ, W, and $\langle 1/r^3\rangle$ vary only smoothly with the impurity and host. However, they determine only the possible magnitude of the effect. The actual value of the noncubic charge distribution varies within this frame rather strongly with the band filling and form of the band structure. This becomes apparent in the systematics as a strong dependence on the impurity and host: The change in the SO-EFG from one impurity or one host to the next is often of the same order of magnitude as the SO-EFG itself. The systematics is thus a sensitive probe of the evolution of the local electronic structure within the $5d$ impurities.

The strong variation of the effect is theoretically well understood. For example, it is shown in part II that the effect passes through at least three sign changes as the conduction band is filled. This implies a sign change at least every 2.5 d electrons and explains already a large part of the observed variation.

For a detailed discussion of the systematics the local densities of states should at least be approximately known. The discussion of the $5d$ impurities in Co(fcc) and Ni must, therefore, be postponed until such calculations become available.

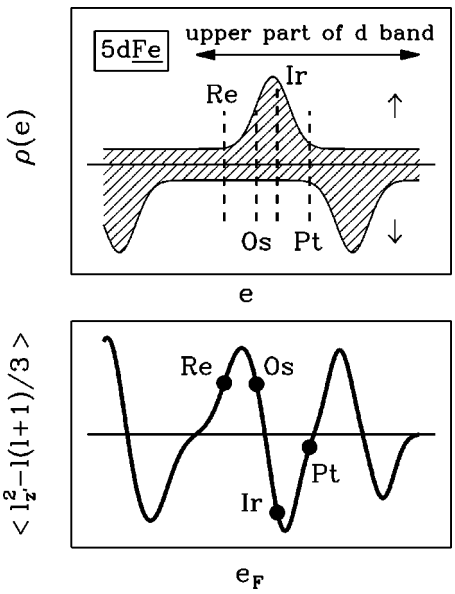

FIG. 18. Interpretation of the observed systematics for the $5d$ impurities in Fe as a band filling effect. The top and bottom parts schematically show the common pattern in the density of states and in the dependence of the noncubic charge distribution on the Fermi energy, respectively. (Most of the lower part of the d band is omitted.) The dashed lines and solid circles represent a set of Fermi energies that reproduces roughly the experimental trend.

The band structure of the $5d$ impurities in Fe, however, has been investigated in part II of this work. It turned out that these systems show a common basic pattern in the density of states and in the dependence of the noncubic charge distribution on the band filling. These patterns are shown schematically in Fig. 18: The $5d$ band shows a marked separation into a bonding (lower) and an antibonding (upper) part. The spin-up band lies in each part somewhat lower than the spin-down band. As the band is successively filled the noncubic charge distribution is in each part of the band first positive, then negative, then positive, and at last negative again. The general trend of the systematics is determined by the successive rise of the Fermi energy within this pattern with increasing atomic number of the impurity.

Although the model calculations in part II fail to reproduce the SO-EFG's of the individual $5d$ impurities in Fe, the just-described band filling scheme should nevertheless be correct. Therefore, we propose that the Fermi energies are actually positioned in this scheme somewhat more to the left than calculated in part II. These modified positions are shown in Fig. 18. They were chosen in such a way that the experimental signs and relative magnitudes of the noncubic charge distribution are moderatly well reproduced, that the Fermi energy rises continually from Re to Pt, and that the complete picture is as similar as possible to the one given in part II. Of course, this interpretation of the systematics is at the present stage rather speculative.

In Fig. 18 it is assumed that IrFe lies near a maximum of the noncubic charge distribution. As mentioned above, this is at variance with our model calculations in part II. They predict that the maximum noncubic charge distribution is about three times larger than the experimental noncubic charge dis-

TABLE XIV. SO-EFG ratios in Fe and Ni from this work and Refs. 22, 23, 28, and 36.

System	$V_{z'z'}^{[100]}/V_{z'z'}^{[111]}$	$V_{z'z'}^{[100]}/V_{z'z'}^{[110]}$	$(V_{z'z'}^{[110]}-V_{z'z'}^{[111]})/(V_{z'z'}^{[100]}-V_{z'z'}^{[111]})$
Au*Fe*	1.99(14)	1.52(6)	0.31(6)
Pt*Fe*	0.35(12)	0.42(15)	0.27(7)
Ir*Fe*	1.855(13)	1.556(19)	0.226(23)
Os*Fe*	1.49(5)	1.38(8)	0.15(13)
Re*Fe*	1.14(4)	1.11(6)	0.21(32)
Pt*Ni*	0.909(9)	0.930(8)	0.25(9)
Ir*Ni*	0.425(12)	0.458(13)	0.124(10)

tribution of Ir*Fe*. If we would have assumed the latter, all systems in Fig. 18 would have to lie relatively near a zero crossing and the increase of the Fermi energy would be rather discontinuous: The increase from Os to Ir would be much smaller than from Re to Os or from Ir to Pt. This is a further hint that the model calculations overestimate the typical magnitude of the noncubic charge distribution.

Despite the crude nature of our interpretation of the systematics, it shows already that Au*Fe* must be a special case: From the systematics up to Pt clearly a sign change between Pt*Fe* and Au*Fe* is expected, which is, however, not observed in the experiment.

D. Anisotropy of the noncubic charge distribution

The data on the anisotropy are compiled in Table XIV in the form of several EFG ratios. The variation of the effect between $M\|[100]$ and $M\|[111]$ depends strongly on the particular system and ranges from about 10% for Pt*Ni* and Re*Fe* up to about a factor of 2.5 for Pt*Fe* and Ir*Ni*. For Au*Ni* the noncubic charge distribution changes even the sign (see Table X). The model calculations in part II show that this is the range of anisotropies that is expected for realistic band structures.

The distinct dependence of the noncubic charge distribution on the direction of the magnetization is a consequence of the nonspherical symmetry of the band structure, which manifests itself for a cubic symmetric d band in different partial densities of states for the e_g and the t_{2g} orbitals. The e_g and t_{2g} states contribute with different weight according to the orientation of the magnetization: In short, the e_g orbitals are somewhat more important for $M\|[100]$, the t_{2g} orbitals more for $M\|[111]$.[25] The anisotropy probes thus in first line the different distribution of the e_g and t_{2g} states over the band.

The anisotropy of the noncubic charge distribution is not surprising in view of the clear differences between the e_g and t_{2g} densities of states in realistic band structures. Nevertheless, this point was not clear for a long time: Experiments on Ir in Fe and Ni reported the SO-EFG to be isotropic within 10%.[2,5] Our experiments show now for just these two systems large anisotropies of the quadrupole splitting, which are discernible even in the NMR spectrum. The supposed isotropy was theoretically justified in Ref. 6 in terms of the relative strength of the SOC and the crystal potential. This was based, however, on an unrealistic model of the band structure, as is shown in part II of this work. In contrast, the tight-binding calculations from Ref. 7 predicted, for Ir*Ni*, $V_{z'z'}^{[100]} \approx (1/2) V_{z'z'}^{[111]}$. This now turns out to be remarkably close to the experiment.

For a detailed discussion of the anisotropy the partial densities of states should at least be approximately known. Therefore, we can discuss here only the $5d$ impurities in Fe. The partial densities of states of these systems were investigated in part II.

The experimental trend in Fe is that, with the exception of Pt*Fe*, the noncubic charge distribution is larger for $M\|[100]$ than for $M\|[111]$. This is interpreted in part II as an intrinsic property of the bcc lattice: In bcc band structures the e_g states are concentrated in the upper half of the d band in prominent density of states peaks. A concentration of states will in general enlarge the noncubic charge distribution. Since e_g states are mainly concerned, the effect is particularly prominent for $M\|[100]$.

The exception Pt*Fe* confirms this interpretation: Changes in the sign of the noncubic charge distribution will, as a function of the band filling, in general not occur at exactly the same number of electrons for $M\|[100]$ and $M\|[111]$. Therefore, the ratio of $V_{z'z'}^{[100]}$ to $V_{z'z'}^{[111]}$ passes near a sign change necessarily through a wide range of values, irrespective of the general trend. Pt*Fe* seems to be just such a case: The anisotropy is opposite to the general trend, but at the same time the noncubic charge distribution is also particularly small.

The dependence on the direction of the magnetization has in lowest-order perturbation theory the following form[25]:

$$V_{z'z'}([\alpha_x \alpha_y \alpha_z]) = V_{z'z'}^{(0)} + V_{z'z'}^{(2)}(\alpha_x^2\alpha_y^2 + \alpha_y^2\alpha_z^2 + \alpha_z^2\alpha_x^2). \tag{11}$$

The α_i's are the directional cosines between the direction of the magnetization and the cubic axes. The maximum and minimum effects are found for $M\|[100]$ and $M\|[111]$. The complete angular dependence can thus be described by two coefficients $V_{z'z'}^{(0)}$ and $V_{z'z'}^{(2)}$, which are given in terms of the [100] and [111] EFG's by

$$V_{z'z'}^{(0)} = V_{z'z'}^{[100]},$$

$$V_{z'z'}^{(2)} = 3(V_{z'z'}^{[111]} - V_{z'z'}^{[100]}).$$

Equation (11) should hold as long as the SOC strength is small relative to the characteristic energy scale of the band structure. This condition is only moderately well fulfilled for the relatively large SOC strengths of the $5d$ elements. Nevertheless, Eq. (11) may be still a good approximation, since it is just the most simple angular dependence that is consistent with the cubic lattice symmetry.

Equation (11) predicts the position of the [110] EFG with respect to the [100] and [111] EFG's. As a linear measure of this position we define the EFG ratio κ:

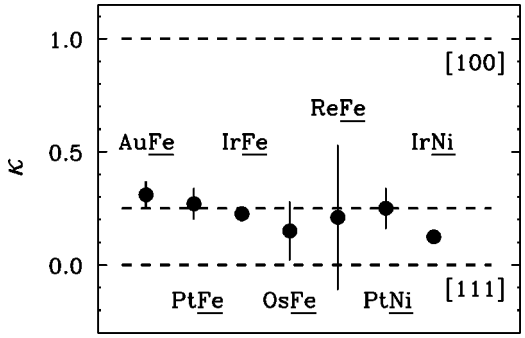

FIG. 19. Position of the [110] EFG with respect to the [100] and [111] EFG's for several $5d$ impurities in Fe and Ni. κ is defined in Eq. (12). The lowest-order prediction is $\kappa=1/4$.

$$\kappa=\frac{V_{z'z'}^{[110]}-V_{z'z'}^{[111]}}{V_{z'z'}^{[100]}-V_{z'z'}^{[111]}}. \tag{12}$$

κ equals 0 for $V_{z'z'}^{[110]}=V_{z'z'}^{[111]}$ and 1 for $V_{z'z'}^{[110]}=V_{z'z'}^{[100]}$. Equation (11) predicts that $\kappa=1/4$. $V_{z'z'}^{[110]}$ should thus be 3 times closer to $V_{z'z'}^{[111]}$ than to $V_{z'z'}^{[100]}$. Figure 19 shows the experimental κ's: Equation (11) describes correctly the position of the [110] EFG within the experimental error for almost all systems. A significant deviation is found only for IrNi.

Deviations from Eq. (11), as found here for IrNi, are of interest as deviations from lowest-order perturbation theory: In lowest-order perturbation theory only the band structure in the absence of the SOC and the parameter ξ are important. However, it would be interesting for the theory of the SOC in metals whether the more spin-orbit-specific higher-order effects are also correctly described. Higher-order effects arise when the SOC strength becomes of the same order of magnitude as the energy splitting of the states that are mixed by the SOC or when the SOC itself changes appreciably the band structure. Higher-order effects can be separated in calculations simply by varying the SOC strength and observing the deviations from the behavior at low SOC strengths. Appropriate techniques to vary the SOC strength within *ab initio* calculations have recently been developed.[46] However, to probe selectively only the higher-order effects in the experiment, a quantity is needed that is known exactly in lowest order. κ is such a quantity.

Figures 11 and 16 show the complete angular dependence of the noncubic charge distribution in the (110) plane for PtNi and IrNi. One finds a smooth variation of the noncubic charge distribution between $M\|[100]$, $M\|[110]$, and $M\|[111]$. This is expected since the different weightings of the e_g and t_{2g} orbitals can change only slowly as a function of the direction of the magnetization, even if Eq. (11) is no longer valid.

The position of the [110] EFG already showed that Eq. (11) fails to describe the form of the anisotropy for IrNi. The next-higher-order polynomial in the α_i's has the form

$$V_{z'z'}([\alpha_x\alpha_y\alpha_z])=V_{z'z'}^{(0)}+V_{z'z'}^{(2)}(\alpha_x^2\alpha_y^2+\alpha_y^2\alpha_z^2+\alpha_z^2\alpha_x^2)+V_{z'z'}^{(3)}(\alpha_x^2\alpha_y^2\alpha_z^2). \tag{13}$$

TABLE XV. Absolute and relative anisotropy of the magnetic hyperfine field in cubic Fe and Ni.

System	$B_{\mathrm{HF}}^{[100]}-B_{\mathrm{HF}}^{[111]}$ (T)	$\frac{B_{\mathrm{HF}}^{[100]}-B_{\mathrm{HF}}^{[111]}}{B_{\mathrm{HF}}^{[100]}}$ (10^{-3})	Ref.
PtFe	0.00(8)	0.0(6)	28
IrFe	−0.11(5)	+0.8(4)	22,36
OsFe	+0.19(16)	−1.6(14)	a
ReFe	+0.04(7)	−0.5(10)	a
PtNi	0.00(2)	0.0(5)	a
IrNi	+0.05(3)	−1.1(7)	a

[a]This work.

The coefficients are given in terms of the [100], [110], and [111] EFG's by

$$V_{z'z'}^{(0)}=V_{z'z'}^{[100]},$$

$$V_{z'z'}^{(2)}=4(V_{z'z'}^{[110]}-V_{z'z'}^{[100]}),$$

$$V_{z'z'}^{(3)}=9(3V_{z'z'}^{[111]}-4V_{z'z'}^{[110]}+V_{z'z'}^{[100]}).$$

This form of the anisotropy is compared with the experiment in Fig. 16: It turns out that for IrNi even this three-parameter interpolation deviates slightly from the experimental angular dependence.

No data on the anisotropy are available for the light impurities. However, a similar range of anisotropies is expected for the $3d$ and $4d$ impurities as for the $5d$ impurities, because the anisotropy is in lowest order independent of ξ, and the differences between the e_g and t_{2g} densities of states are similar for the $3d$, $4d$, and $5d$ systems. On the contrary, no anisotropy is expected for the sp impurities since all three p orbitals have the same density of states in cubic band structures.

E. Anisotropy of the hyperfine field

In all experiments we also measured the magnetic hyperfine splitting for different directions of the magnetization. Table XV compiles the respective anisotropies of the magnetic hyperfine field. The magnetic hyperfine field turns out to be isotropic within the typical experimental error of 0.1 T (absolute error) or 1×10^{-3} (relative error). A similarly perfect isotropy is also known from the magnetization of Fe and Ni, which is isotropic within 10^{-4}.[47,48]

This isotropy is in marked contrast to the anisotropy of the SO-EFG, in particular since there are also orbital contributions to the hyperfine field and the magnetization of the order of several percent.[29,49] As discussed in part II, this different behavior is a special property of the cubic lattice symmetry and is well understood: The orbital hyperfine field is in fact anisotropic but only in higher-order perturbation theory, since the cubic lattice symmetry allows in first-order perturbation theory no anisotropy of the orbital moment. The second potentially anisotropic contribution to the hyperfine

field is the spin-dipolar field that arises from the spin-orbit induced noncubic spin distribution. The latter is, as its counterpart, the noncubic charge distribution, anisotropic already in lowest-order perturbation theory. But it contributes only about 10^{-3} to the total hyperfine field. Simple order of magnitude estimates show that the anisotropy of the hyperfine field due to the orbital and spin-dipolar contributions should be of the order of several 10^{-4} for the $5d$ impurities.[28]

The accuracy in the comparison of the [100] and [111] hyperfine fields was limited in this work mainly by the estimation of the demagnetization field and the determination of ν_m from NMR-ON spectra with unresolved quadrupole splittings. An accuracy of 1×10^{-4} should be feasible by using thinner samples and selected systems with resolved quadrupole splitting in the NMR-ON spectrum.

F. Inhomogeneous broadening of the noncubic charge distribution

The inhomogeneous broadening of the hyperfine interaction is often used as a rough measure of the disturbance of the lattice in the vicinity of the probe atom. Its recording is, therefore, important for the improvement of the sample preparation and the comparison of different experiments. The broadening of the SO-EFG may, however, be more than that: Its anisotropy seems to be independent of the anisotropy of the SO-EFG. This suggests that the broadening is also sensitive to parameters that are independent of the sample preparation and that it can provide information on the physics of the noncubic charge distribution.

The interpretation of the broadening is at present difficult since virtually nothing is known on the nature of the responsible lattice defects or how they cause the broadening. The mechanism may be the induction of extra EFG's by the disturbance of the cubic lattice symmetry or the modification of the SO-EFG strength by changes in the local band structure. Modification of the SO-EFG strength seems to be more probable since the anisotropy and the Gaussian form of the broadening would be difficult to explain by extra EFG's. The inhomogeneous broadening would in this case provide information on the sensitivity of the quantity noncubic charge distribution to changes of the band structure. In principle, one can also speculate on intrinsic, sample-independent, contributions to the broadening, wherever they may come from (charge density waves, Jahn-Teller effect, dynamic fluctuations in the charge and spin densities, or something else).

Since the origin of the broadening is not known, we will confine ourselves in the following to a short summary of the main experimental facts and leave the interpretation as an open problem. A better understanding of the inhomogeneous broadening of the SO-EFG may arise in the future from more data on the systematics of its anisotropy, from experiments on the same system in samples with different inhomogeneous broadening, from more data on different probe atoms in the same sample, and from experiments with deliberately introduced, well-known impurities.

The most conspicuous experimental fact is the large relative broadening of the EFG distribution: It ranges in our experiments from 10% for Pt*Ni* to more than 100%. This represents an extraordinary sensitivity to disturbances. The absolute width Γ_V of the EFG distributions is compiled in Table XVI. The entries are in principle not directly comparable, since Γ_V depends on the sample preparation. Nevertheless, a common order of magnitude seems to emerge for $5d$ impurities in carefully prepared samples: Γ_V ranges between 0.2×10^{16} V/cm^2 and 1.0×10^{16} V/cm^2. Only $\Gamma_V \approx 0.1\times10^{16}$ V/cm^2 for Pt*Ni* is somewhat smaller.

TABLE XVI. Inhomogeneous broadening of the EFG distribution for several Fe and Ni experiments.

System	Γ_V (10^{16} V/cm^2) $M\|[100]$	$M\|[110]$	$M\|[111]$	Ref.
Pt*Fe*	0.58(12)	0.37(4)	0.21(2)	23
Ir*Fe*	0.64(12)	0.66(10)	0.42(13)	22
	0.66(3)		0.38(2)	36
Os*Fe*	0.94(10)	0.68(8)	0.53(5)	a
Re*Fe*	1.03(11)	0.75(12)	0.46(5)	a
Pt*Ni*	0.08(3)		0.10(2)	a
Ir*Ni*	0.94(5)	0.53(3)	0.31(3)	a

[a]This work.

Re*Fe* and Os*Fe* represent a special case: The measurements were performed in the same sample on the same lattice sites. The broadenings are thus directly comparable and it is found that they agree within the experimental error. This may point to a system unspecific broadening of the EFG, but much more data are required to postulate such an effect.

The anisotropy of the inhomogeneous broadening is of the same order of magnitude as the anisotropy of the SO-EFG: Γ_V varies by up to a factor of 3 between $M\|[100]$ and $M\|[111]$. The anisotropy has the same (Ir*Fe*,Os*Fe*) or the opposite (Pt*Fe*,Ir*Ni*) sign as the anisotropy of the SO-EFG. The inhomogeneous broadening behaves in this respect like an independent spin-orbit effect. The trend in Fe is that Γ_V is considerably larger for $M\|[100]$ than for $M\|[111]$. This trend was already observed for $V_{z'z'}$ and may have the same origin: A general trend to larger SO-EFG's for $M\|[100]$ should also lead to larger variations of the SO-EFG in response to disturbances.

VI. CONCLUSIONS

The two parts of this work investigate the spin-orbit induced effect of the noncubic charge distribution in cubic Fe, Co, and Ni both experimentally, by EFG measurements on $5d$ impurities, and theoretically, within the tight-binding model.

The EFG measurements in part I complete the recent reinvestigation of the SO-EFG at the $5d$ impurities. These new data are summarized in this work. It is the first accurate and complete data set on the SO-EFG: Previously, the effect could be determined only for a few selected systems and was assumed to be essentially isotropic. Now, it is known for a continuous series of $5d$ impurities and has been determined in Fe and Ni for at least three different orientations of the magnetization.

A transparent and yet realistic tight-binding treatment of

the SO-EFG was developed in part II. The basic properties of the noncubic charge distribution and its relation to the band structure were investigated within this scheme and are now qualitatively well understood. On the contrary, the previously accepted qualitative interpretation of the effect was based on an unrealistic model and turned out to be partially incorrect.

Our study also showed that the quantity SO-EFG can indeed make important contributions to the understanding of the spin-orbit effects in transition metals. The main features of the effect in this context are the following.

(i) The noncubic charge distribution arises in second-order perturbation theory. It provides thus complementary information to the more often studied first-order effects, like the orbital moment or Kerr effect, and to the more complex, higher-order effects, like the anisotropy energy or magnetostriction. Moreover, the effect can in principle be measured for a wide range of impurities. Decisive parameters like the SOC strength and the symmetry of the electrons can be varied in this way in a controlled manner over a wide range.

(ii) The effect is also an ideal probe of the local band structure of the particular system: On the one hand, it is sensitive to the local electronic structure. (This is not a matter of course: The hyperfine field, for example, shows no sign change from Lu to Hg, although the sign of both the spin and orbital moment changes in this series.[49,50]) But the sensitivity to band structure details is also not too large: Calculations that reproduce the main features in the density of states should also be able to reproduce the systematics of the SO-EFG.

(iii) The noncubic charge distribution provides a lot of information: Its magnitude is sensitive to the interaction between the SOC and band structure, its systematics is sensitive to the band structure, its anisotropy is sensitive to the different distributions of e_g and t_{2g} states, the exact form of its anisotropy is sensitive to deviations from perturbation theory, and its inhomogeneous broadening may be a general measure of the sensitivity to disturbances of the band structure.

Several schemes were recently developed to treat the SOC self-consistently within *ab initio* calculations.[51–53] It would be interesting to test these schemes by the SO-EFG data. However, no *ab initio* calculations on the SO-EFG were reported so far.

The experimental investigation of the effect is also still at the beginning: The $5d$ impurities were a convenient starting point because of the unproblematic implantation behavior and the large SOC strength. However, precise SO-EFG data would also be desirable for smaller ($3d$,$4d$ impurities) and larger ($6sp$ impurities) SOC strengths, for a dominant p character of the conduction electrons (sp impurities), for systems with pronounced local moments ($3d$ impurities), and for the pure systems Fe, Co(fcc), and Ni, which are well known from a multitude of other studies.

ACKNOWLEDGMENTS

We wish to thank Professor H.-J. Körner for his continuous interest and support of this work. We appreciate very much the effort made by the ISOLDE and Orsay group for the development of the liquid Pb target. We also wish to thank Dr. J. Völkl, W. Clauss, G. Neff, H. Schneider, M. Stanger, and H. Utz of the Kristall-Labor for support in the preparation of the single crystals and E. Smolic for experimental help. The work has been funded by the Deutsche Forschungsgemeinschaft (DFG) under Contract No. Ha 1282/3-3.

[1] M. Aiga and J. Itoh, J. Phys. Soc. Jpn. **31**, 1844 (1971).
[2] P. D. Johnston and N. J. Stone, J. Phys. C **5**, L303 (1972).
[3] R. L. Mössbauer, M. Lengsfeld, W. v. Lieres, W. Potzel, P. Teschner, F. E. Wagner, and G. Kaindl, Z. Naturforsch. A **26**, 343 (1971).
[4] J. J. Spijkerman, J. C. Travis, D. N. Pipkorn, and C. E. Violet, Phys. Rev. Lett. **26**, 323 (1971).
[5] M. Aiga and J. Itoh, J. Phys. Soc. Jpn. **37**, 967 (1974).
[6] G. A. Gehring and H. C. W. L. Williams, J. Phys. F: Met. Phys. **4**, 291 (1974).
[7] C. Demangeat, J. Phys. F: Met. Phys. **5**, 169 (1975).
[8] P. C. Riedi and E. Hagn, Phys. Rev. B **30**, 5680 (1984).
[9] M. Kawakami, H. Enokiya, and T. Okamoto, J. Phys. F: Met. Phys. **15**, 1613 (1985).
[10] H. Enokiya and M. Kawakami, J. Phys. Soc. Jpn. **50**, 2221 (1981).
[11] P. T. Callaghan, P. J. Back, D. H. Chaplin, H. R. Foster, and G. V. H. Wilson, Hyperfine Interact. **22**, 39 (1985).
[12] P. T. Callaghan, P. J. Back, and D. H. Chaplin, Phys. Rev. B **37**, 4900 (1988).
[13] D. H. Chaplin, W. D. Hutchison, M. P. Kopp, and N. Yazidjoglou, Hyperfine Interact. **43**, 241 (1988).
[14] N. Yazidjoglou, W. D. Hutchison, and D. H. Chaplin, Hyperfine Interact. **61**, 1419 (1990).
[15] N. Yazidjoglou, W. D. Hutchison, and G. A. Stewart, J. Phys.: Condens. Matter **6**, 7109 (1994).
[16] W. D. Hutchison, N. Yazidjoglou, and D. H. Chaplin, Aust. J. Phys. **51**, 295 (1998).
[17] P. J. Back, D. H. Chaplin, and P. T. Callaghan, Phys. Rev. B **37**, 4911 (1988).
[18] P. J. Back, Z. Nawaz, and N. J. Stone, Hyperfine Interact. **51**, 909 (1989).
[19] P. J. Back, Hyperfine Interact. **43**, 211 (1988).
[20] H. Richter, diploma thesis, TU München, 1993.
[21] J. Zeiner, diploma thesis, TU München, 1994.
[22] G. Seewald, E. Hagn, E. Zech, D. Forkel-Wirth, A. Burchard, and ISOLDE Collaboration, Phys. Rev. Lett. **78**, 1795 (1997).
[23] G. Seewald, E. Hagn, E. Zech, R. Kleyna, M. Voß, D. Forkel-Wirth, A. Burchard, and ISOLDE Collaboration, Phys. Rev. Lett. **82**, 1024 (1999).
[24] G. Seewald, E. Hagn, and E. Zech, Phys. Rev. B **63**, 054428 (2001).
[25] G. Seewald, E. Zech, and H. Haas, following paper, Phys. Rev. B **66**, 174402 (2002).

[26] G. A. Gehring, Phys. Scr. **11**, 215 (1974).
[27] E. Matthias and R. J. Holliday, Phys. Rev. Lett. **17**, 897 (1966).
[28] G. Seewald, Ph.D. thesis, TU München, 1999.
[29] M. B. Stearns, in *Magnetic Properties of Metals*, edited by H. P. Wijn, Landolt-Börnstein, New Series, Group III, Vol. 19a (Springer, Berlin, 1986).
[30] E. Hagn and E. Zech, Z. Phys. A **295**, 345 (1980).
[31] T. Dumelow, P. C. Riedi, E. Hagn, and E. Zech, Phys. Rev. C **54**, 2310 (1996).
[32] H. D. Rüter, E. W. Duczynski, W. Haaks, and E. Gerdau, Hyperfine Interact. **11**, 37 (1981).
[33] M. Kontani and J. Itoh, J. Phys. Soc. Jpn. **22**, 345 (1967).
[34] Th. Hilberath, St. Becker, G. Bollen, H.-J. Kluge, U. Krönert, G. Passler, J. Rikovska, R. Wyss, and ISOLDE Collaboration, Z. Phys. A **342**, 1 (1992).
[35] E. Hagn and E. Zech, Z. Phys. A **297**, 329 (1980).
[36] G. Seewald, E. Zech, H.-J. Körner, M. Dietrich, and ISOLDE Collaboration (unpublished).
[37] E. Hagn, K. Leuthold, E. Zech, and H. Ernst, Z. Phys. A **295**, 385 (1980).
[38] G. Seewald, E. Hagn, B. Hinfurtner, E. Zech, D. Forkel-Wirth, R. Eder, and ISOLDE Collaboration, Phys. Rev. Lett. **77**, 5016 (1996).
[39] E. Hagn, Hyperfine Interact. **22**, 19 (1985).
[40] G. Seewald, E. Zech, E. Hagn, H.-J. Körner, P. Herzog, C. Tramm, and K. Freitag (unpublished).
[41] P. Dufek, P. Blaha, and K. Schwarz, Phys. Rev. Lett. **75**, 3545 (1995).
[42] W. D. Hutchison, A. V. J. Edge, N. Yazidjoglou, and D. H. Chaplin, Hyperfine Interact. **75**, 291 (1992).
[43] D. H. Chaplin and W. D. Hutchison, Hyperfine Interact. **75**, 209 (1992).
[44] S. Fraga, J. Karwowski, and K. M. S. Saxena, *Handbook of Atomic Data* (Elsevier, Amsterdam, 1976).
[45] T. Asada, K. Terakura, and T. Jarlborg, J. Phys. F: Met. Phys. **11**, 1847 (1981).
[46] H. Ebert, H. Freyer, A. Vernes, and G.-Y. Guo, Phys. Rev. B **53**, 7721 (1996).
[47] R. Pauthenet, J. Appl. Phys. **53**, 2029 (1982).
[48] P. Escudier, Ann. Phys. (Paris) **9**, 125 (1975).
[49] H. Ebert, R. Zeller, B. Drittler, and P. H. Dederichs, J. Appl. Phys. **67**, 4576 (1990).
[50] D. H. Akai, Hyperfine Interact. **43**, 255 (1988).
[51] O. Eriksson, L. Nordström, A. Pohl, L. Severin, A. M. Boring, and B. Johansson, Phys. Rev. B **41**, 11 807 (1990).
[52] H. Ebert, M. Battocletti, and E. K. U. Gross, Europhys. Lett. **40**, 545 (1997).
[53] T. Huhne, C. Zecha, H. Ebert, P. H. Dederichs, and R. Zeller, Phys. Rev. B **58**, 10 236 (1998).